

# Flexible and efficient spatial extremes emulation via variational autoencoders

Likun Zhang<sup>1</sup>, Xiaoyu Ma<sup>1</sup>, Christopher K. Wikle<sup>1</sup>, and Raphaël Huser<sup>2</sup>

<sup>1</sup>Department of Statistics, University of Missouri, Columbia, Missouri 65211, USA

<sup>2</sup>Statistics Program, Computer, Electrical and Mathematical Sciences and Engineering (CEMSE) Division, King Abdullah University of Science and Technology (KAUST), Thuwal 23955-6900, Saudi Arabia

## Abstract

Many real-world processes have complex tail dependence structures that cannot be characterized using classical Gaussian processes. More flexible spatial extremes models such as Gaussian scale mixtures and single-station conditioning models exhibit appealing extremal dependence properties but are often exceedingly prohibitive to fit and simulate from. In this paper, we develop a new spatial extremes model that has flexible and non-stationary dependence properties, and we integrate it in the encoding-decoding structure of a variational autoencoder (extVAE). The extVAE can be used as a spatio-temporal emulator that characterizes the distribution of potential mechanistic model output states and produces outputs that have the same properties as the inputs, especially in the tail. Through extensive simulation studies, we show that our extVAE is vastly more time-efficient than traditional Bayesian inference while also outperforming many spatial extremes models with a stationary dependence structure. To further demonstrate the computational power of the extVAE, we analyze a high-resolution satellite-derived dataset of sea surface temperature in the Red Sea, which includes daily measurements at 16703 grid cells.

*Keywords:* Asymptotic dependence, Extreme value theory, Max-infinitely divisible process, Neural network, Spatial statistics, Weather emulation

## 1 Introduction

Large mechanistic-based simulation models are crucial for understanding complex problems related to energy and the environment. These models are ubiquitous in science and engineering. For example, earth system models couple complex climate models with physical, chemical, and biological models that include interactions between ocean, atmosphere, sea ice, the biosphere along with human population effects. Each component model in such systems is typically computationally expensive to run and, when combined, the computational and uncertainty quantification (UQ) challenges can be quite formidable. Examples

of other related challenges include model calibration, inverse problems, UQ for forward simulations, and the specification of realistic model parameterizations for coupled processes. Surrogate model emulators (e.g., see the overview in [Gramacy, 2020](#)) have proven to be useful in recent years to facilitate UQ in these contexts, particularly when combined with Bayesian inference ([Kennedy and O’Hagan, 2001](#)).

In many cases, the most important outcome of a complex simulation model is the accurate simulation of the occurrence, intensity and spatial extent of simultaneous large-scale extreme events (e.g., mega-wildfires, drought, floods, pandemics, etc.) Planning associated with such extremes is always challenging given that one is interested in estimating events at the tails of the distribution, which is especially difficult under non-stationarity, for example, due to the changing climate. Thus, it is of great importance to develop emulators for state-of-the-art simulation models, e.g., in the context of climate models, the HighResMIP v1.0 product for CMIP6 ([Haarsma et al., 2016](#)) and the regionally refined E3SM ensemble simulations ([Golaz et al., 2019](#)). Surrogate models seek to emulate such complex deterministic models so that, given some inputs, the emulator produces realistic outputs with much less computational expense (see [Gramacy, 2020](#), for an overview), thereby allowing one to explore many more input scenarios. In most cases, these extreme events are dependent in space and time (e.g., drought in the desert southwest that lasts multiple years). Traditional methods for model emulation such as Gaussian processes (e.g., [Gu et al., 2018](#)), polynomial chaos expansions (e.g., [Sargsyan, 2017](#)), and more recently, deep neural networks (e.g., [Kasim et al., 2020](#)) and generative models such as generative adversarial networks, or GANs, and variational autoencoders, or VAEs, do not naturally accommodate extreme values, and certainly not dependent extreme values. The focus of this paper is to develop the first rigorous surrogate modeling framework that can accommodate dependent extremes in a flexible statistical framework that allows for uncertainty quantification.

Previously, [Allouche et al. \(2021\)](#) and [Allouche et al. \(2022\)](#) embedded univariate extreme value theory in a feedforward neural network and in the generator of a GAN (called EV-GAN), respectively, to approximate the tail index function and the quantile function of a heavy-tailed distribution. In the spatial setting, [Boulaguiem et al. \(2022\)](#) analyzed the block maxima data in a pointwise manner to obtain the marginal GEV parameter estimates, and then transform the observations into the uniform scale and trained a deep convolutional GAN (called extGAN) to learn and emulate the dependence structure. However, classical GANs do not impose any structure justified by extreme value theory and do not account for spatial extremal dependence. For a spatial process that exhibits asymptotic dependence, extGAN might thus underestimate the intensity and length scale of simultaneous extreme events. [McDonald et al. \(2022\)](#) and [Lafon et al. \(2023\)](#) built similar emulators based on extreme value theory and on copulas with multivariate regular variation, but they are difficult to extend to emulate higher dimensional spatial data sets. In this work, we first develop a novel spatial extremes model that has flexible nonstationary dependence properties to explicitly accommodate concurrent and locally dependent extremes. We then embed this flexible spatial extremes model within a variational autoencoder ([Kingma and Welling, 2013](#), VAE) engine for enabling fast and efficient model calibration and data emulation with uncertainty quantification. We also propose a new validation framework that

is tailored to assessing skill in fitting extremal behavior of model outputs.

The paper proceeds as follows. First, in Section 2, we propose a novel max-infinitely divisible (max-id) process that has highly flexible extremal dependence properties. Next, Section 3 details our extVAE and how we embed the proposed max-id process into the encoder-decoder VAE construction. Section 5 validates the emulating power of our extVAE by simulation using various scoring rules and demonstrates its advantages over the commonly used Gaussian process emulators. Then, in Section 6, we apply our extVAE to analyze high-resolution Red Sea surface temperatures. Lastly, in Section we conclude the paper and discuss perspectives for future work.

## 2 Flexible spatial extremes model

Many spatial extremes models have been developed to be expressive enough to capture the simultaneous occurrence of extreme events, with a specific focus on accurately characterizing the joint tail decay rate in different parts of the input domain. Similar to variograms, the extremal dependence structure is commonly described by the bivariate measure

$$\chi_{12}(u) = \Pr\{F_2(X_2) > u \mid F_1(X_1) > u\} = \frac{\Pr\{F_2(X_2) > u, F_1(X_1) > u\}}{\Pr\{F_1(X_1) > u\}}, \quad (1)$$

in which  $u \in (0, 1)$  and  $X_1$  and  $X_2$  are two variables with continuous marginal distribution function  $F_1$  and  $F_2$ , respectively. In the spatial case,  $X_1 = X(\mathbf{s}_1)$  and  $X_2 = X(\mathbf{s}_2)$  are two observations from a process  $\{X(\mathbf{s}); \mathbf{s} \in \mathcal{D} \subset \mathbb{R}^2\}$  at spatial locations  $\mathbf{s}_1$  and  $\mathbf{s}_2$ . When  $u$  is close to one,  $\chi(u)$  quantifies the probability that one variable is extreme given that the other variable is similarly extreme. If  $\chi_{12} = \lim_{u \rightarrow 1} \chi_{12}(u) = 0$ ,  $X_1$  and  $X_2$  are said to be *asymptotically independent* (AI), and if  $\chi_{12} = \lim_{u \rightarrow 1} \chi_{12}(u) > 0$ ,  $X_1$  and  $X_2$  are *asymptotically dependent* (AD). Max-stable or generalized Pareto processes (de Haan and Ferreira, 2006; Ferreira and de Haan, 2014; Thibaud and Opitz, 2015) have the property that  $\chi_{12}$  is always positive (Huser and Wadsworth, 2020). On the other hand, Gaussian processes (or multivariate Gaussian distributions) have the property that  $\chi_{12}(u)$  always converges to 0, unless  $X_1$  and  $X_2$  are exactly dependent.

In contrast, tail dependence in observed environmental processes often seems to decay as events get more extreme and rare events often tend to be more spatially localized as the intensity increases. This was observed in numerous studies, including threshold exceedances of three-hourly wave height data (Huser and Wadsworth, 2019), daily Fosberg fire index (Zhang et al., 2022b), winter maximum precipitation data over the Midwest of the U.S. (Zhang et al., 2022a), and 5 day-cumulative winter precipitation over the contiguous U.S. (Castro-Camilo and Huser, 2020). The stability property of max-stable and generalized Pareto models is thus often a physically inappropriate restriction in the joint tail. However, a weakening  $\chi_{12}(u)$  as  $u$  increases does not necessarily lead to AI. As we try to extrapolate into the joint tail beyond the observed data, mis-classifying the tail dependence regime inevitably leads to inaccurate risk assessments. Therefore, we seek models that exhibit much more flexible tail characteristics and do not impose a dependence class *a priori*, so it can be learned from the data rather than imposed by the model.

## 2.1 Model definition

We first propose a flexible spatial extremes model that can easily be integrated in a VAE and that has space-scale aware and non-stationary dependence properties. Traditionally, most spatial extremes models such as max-stable and generalized Pareto processes can only exhibit one extremal dependence class, which might lead to an overestimation or underestimation of the risks associated with simultaneous occurrences of extremes across the spatial domain (Huser and Wadsworth, 2022). By contrast, our model builds upon the max-infinitely divisible (max-id) process proposed by Reich and Shaby (2012) and Bopp et al. (2021), which is modified to allow for both short-range asymptotic dependence along with long-range asymptotic independence. The modified model can be specified as follows:

$$X(\mathbf{s}) = \epsilon(\mathbf{s})Y(\mathbf{s}), \quad \mathbf{s} \in \mathcal{S}, \quad (2)$$

where  $\mathcal{S} \in \mathbb{R}$  is the domain of interest and  $\epsilon(\mathbf{s})$  is a white noise process with independent Fréchet(0,  $\tau$ ,  $1/\alpha_0$ ) marginal distribution. That is,  $\Pr\{\epsilon(\mathbf{s}) \leq x\} = \exp\{-(x/\tau)^{1/\alpha_0}\}$ ,  $x > 0$ ,  $\alpha_0 > 0$ , and  $Y(\mathbf{s})$  is constructed through a low-rank representation:

$$Y(\mathbf{s}) = \left\{ \sum_{k=1}^K \omega_k(\mathbf{s}, r_k)^{\frac{1}{\alpha}} Z_{kt} \right\}^{\alpha_0}. \quad (3)$$

Here, we use compactly-supported Wendland basis functions  $\omega_k(\mathbf{s}, r_k)$ ,  $k = 1, \dots, K$ , which are centered at  $K$  pre-specified knots  $\{r_k : k = 1, \dots, K\}$  (Wendland, 1995), and the latent variables are lighter-tailed, exponentially tilted, positive-stable (PS) variables (Hougaard, 1986):

$$Z_{kt} \stackrel{\text{ind}}{\sim} H(\alpha, \alpha, \theta_k), \quad k = 1, \dots, K, \quad (4)$$

in which the stability parameter  $\alpha \in (0, 1)$  determines the rate at which the tail of  $H(\alpha, \alpha, 0)$  taper off, and larger values of the tilting index  $\theta_k > 0$  induce lighter-tailed distributions of  $Z_{kt}$ . Here, if  $Z \sim H(\alpha, \alpha, 0)$ , it is a positive-stable random variable which has a Laplace transformation of the form  $E\{\exp(-sZ)\} = \exp(-s^\alpha)$ ,  $s \geq 0$ ; see Appendix A.1 for more details.

In Reich and Shaby (2012), the tilting parameters are set to  $\theta_k \equiv 0$ ,  $k = 1, \dots, K$  and the Gaussian radial basis functions are not compactly supported. As a result, their process exhibits max-stability and was used to capture strong, non-vanishing upper tail dependence. In comparison, Bopp et al. (2021) allow the tilting parameters to be positive but still fix it to be constant at all knots. Although they impose an additional log-Gaussian process priors on their radial basis functions, they are still not compactly supported, and hence the spatial process exhibits only asymptotic independence at any pair of locations, even at arbitrarily small distance. Moreover, both Reich and Shaby (2012) and Bopp et al. (2021) set  $\alpha_0 = \alpha$ , while we let  $\alpha_0$  be an extra free parameter to decouple the dependence structure from the marginal tail decay rate.

Another drawback of the processes proposed in Reich and Shaby (2012) and Bopp et al. (2021) is that their white noise process  $\{\epsilon(\mathbf{s})\}$  has independent  $(1/\alpha)$ -Fréchet marginals, i.e., Fréchet(0, 1,  $1/\alpha$ ). Since  $\alpha$  is also the concentration parameter of the exponentially tilted PS variables, the Fréchet(0, 1,  $1/\alpha$ ) variables are usually too noisy compared to the



$\{Y(\mathbf{s})\}$  process with the same  $\alpha$ . In our modification,  $\text{Fréchet}(0, \tau, 1/\alpha_0)$  concentrates around 1 when the shape  $1/\alpha_0 > 1$  and scale  $\tau > 1$ , and then  $\epsilon(\mathbf{s})$  acts as a scaling factor that accounts for measurement errors for each time  $t$ . Furthermore,  $Y(\mathbf{s})$  introduces tail dependence for two close locations covered by the same Wendland basis function. The local dependence strength is proportional to the tail-heaviness of the latent variable at the closest knot. As we will show in Section 2.4, there is local asymptotic dependence if  $\theta_k = 0$ , and there is local asymptotic independence if  $\theta_k > 0$ . In addition, the compactness of the basis function support automatically introduces long-range asymptotic independence for two far-apart stations that are impacted by disjoint sets of basis functions. Therefore, the dependence structure of our model is non-stationary and highly flexible.

## 2.2 Marginal distributions

Now we consider the marginal behavior of our process (2) at the location  $\mathbf{s}_j \in \mathcal{S}$ . For notational simplicity, we denote  $X_j = X(\mathbf{s}_j)$ ,  $\omega_{kj} = \omega_k(\mathbf{s}_j, r_k)$ ,  $k = 1, \dots, K$ ,  $j = 1, \dots, n_s$ , and write  $\mathbf{w}_j = (\omega_{1j}, \dots, \omega_{Kj})$  and  $\mathcal{C}_j = \{k : \omega_{kj} \neq 0, k = 1, \dots, K\}$ . We require that any location  $\mathbf{s} \in \mathcal{S}$  is covered by at least one basis function, thereby  $\mathcal{C}_j$  cannot be empty for any  $j$ .

**Proposition 2.1.** *Let  $\mathcal{D} = \{k : \theta_k = 0\}$  and  $\bar{\mathcal{D}}$  be the complement of  $\mathcal{D}$ . Under the definitions and notations as established in the previous sections, for location  $\mathbf{s}_j$ , the exact form of the marginal distribution function can be written as*

$$F_j(x) = \exp \left[ \sum_{k \in \bar{\mathcal{D}}} \theta_k^\alpha - \sum_{k=1}^K \left\{ \theta_k + \left( \frac{\tau}{x} \right)^{\frac{1}{\alpha_0}} \omega_{kj}^{\frac{1}{\alpha}} \right\}^\alpha \right]. \quad (5)$$

Furthermore, the survival function  $\bar{F}_j(x) = 1 - F_j(x)$  satisfies

$$\bar{F}_j(x) = c'_j x^{-\frac{\alpha}{\alpha_0}} + c_j x^{-\frac{1}{\alpha_0}} + \left( d_j - \frac{c_j^2}{2} \right) x^{-\frac{2}{\alpha_0}} - \frac{c_j'^2}{2} x^{-\frac{2\alpha}{\alpha_0}} - c'_j c_j x^{-\frac{\alpha+1}{\alpha_0}} + o\left(x^{-\frac{2}{\alpha_0}}\right) \quad (6)$$

as  $x \rightarrow \infty$ , in which

$$c_j = \alpha \tau^{\frac{1}{\alpha_0}} \sum_{k \in \bar{\mathcal{D}}} \theta_k^{\alpha-1} \omega_{kj}^{\frac{1}{\alpha}}, \quad c'_j = \tau^{\frac{\alpha}{\alpha_0}} \sum_{k \in \mathcal{D}} \omega_{kj}, \quad d_j = \frac{\alpha(\alpha-1)}{2} \tau^{\frac{2}{\alpha_0}} \sum_{k \in \bar{\mathcal{D}}} \theta_k^{\alpha-2} \omega_{kj}^{\frac{2}{\alpha}}. \quad (7)$$

The proof of this result can be found in Appendix A.2, and it indicates that the process (2) has Pareto-like marginal tails at any location in the domain  $\mathcal{S}$ . If the location is impacted by an un-tilted knot (i.e.,  $\mathcal{C}_j \cap \mathcal{D} \neq \emptyset$ ),  $\bar{F}_j(x) \sim x^{-\frac{\alpha}{\alpha_0}}$  as  $x \rightarrow \infty$  since  $\alpha \in (0, 1)$ . If the location is not within the coverage of an un-tilted knot, the marginal distribution will be less heavy-tailed.

**Corollary 2.1.1.** *Under the assumptions of Proposition 2.1, if  $\mathcal{C}_j \cap \mathcal{D} = \emptyset$ , then  $c'_j = 0$  and*

$$\bar{F}_j(x) = c_j x^{-\frac{1}{\alpha_0}} + \left( d_j - \frac{c_j^2}{2} \right) x^{-\frac{2}{\alpha_0}} + o\left(x^{-\frac{2}{\alpha_0}}\right).$$

The proof of Corollary 2.1.1 is also described in Appendix A.2. To directly delineate how the quantile level changes as  $u \rightarrow 1$ , we derive results on the quantile function  $q_j(t) := F_j^{-1}(1 - 1/t)$ , which are given in the following Corollary and that will be used to prove the dependence results in Section 2.4.

**Corollary 2.1.2.** *Under the assumptions of Proposition 2.1, the marginal quantile function  $q_j(t) = F_j^{-1}(1 - 1/t)$  satisfies*

$$q_j(t) = \begin{cases} c_j^{\alpha_0/\alpha} t^{\alpha_0/\alpha} \left\{ 1 + \frac{\alpha_0 c_j t^{1-1/\alpha}}{\alpha c_j^{1/\alpha}} + \frac{\alpha_0 t^{-1}}{2\alpha} + o(t^{1-1/\alpha}) \right\}, & \text{if } \mathcal{C}_j \cap \mathcal{D} \neq \emptyset, \\ c_j^{\alpha_0} t^{\alpha_0} \left\{ 1 + \alpha_0 \left( \frac{d_j}{c_j^2} - \frac{1}{2} \right) t^{-1} + o(t^{-1}) \right\}, & \text{if } \mathcal{C}_j \cap \mathcal{D} = \emptyset, \end{cases}$$

as  $t \rightarrow \infty$ .

The proof of this results can also be found in Appendix A.2.

## 2.3 Joint distributions

To derive the extremal dependence structure, we first calculate the joint distribution function of a  $n_s$ -variate random vector  $(X_1, \dots, X_{n_s})^T$  drawn from the process (2).

**Proposition 2.2.** *Under the definitions and notations as established in the previous sections, for locations  $\mathbf{s}_1, \dots, \mathbf{s}_{n_s}$ , the exact form of the joint distribution function of the random vector  $(X_1, \dots, X_{n_s})^T$  can written as*

$$F(x_1, \dots, x_{n_s}) = \exp \left[ \sum_{k \in \mathcal{D}} \theta_k^\alpha - \sum_{k=1}^K \left\{ \theta_k + \tau^{\frac{1}{\alpha_0}} \sum_{j=1}^{n_s} \frac{\omega_{kj}^{1/\alpha}}{x_j^{1/\alpha_0}} \right\}^\alpha \right]. \quad (8)$$

The proof of Proposition 2.3 is given in Appendix A.3. Eq. (8) ensures that

$$F^{1/s}(x_1, \dots, x_{n_s}) = \exp \left[ \sum_{k \in \mathcal{D}} \left( \frac{\theta_k}{s^{1/\alpha}} \right)^\alpha - \sum_{k=1}^K \left\{ \frac{\theta_k}{s^{1/\alpha}} + \tau^{\frac{1}{\alpha_0}} \sum_{j=1}^{n_s} \frac{(\omega_{kj}/s)^{1/\alpha}}{x_j^{1/\alpha_0}} \right\}^\alpha \right]$$

is a valid distribution function on  $\mathbb{R}^n$  for any  $s > 0$  with tilting indices  $\{\theta_1/s^{1/\alpha}, \dots, \theta_K/s^{1/\alpha}\}$  and basis values  $\{\omega_{kj}/s : k = 1, \dots, K, j = 1, \dots, n_s\}$ . Therefore, the process  $\{X_t(\mathbf{s}) : \mathbf{s} \in \mathcal{D}\}$  is max-infinitely divisible.

## 2.4 Dependence properties

We now characterize the tail dependence of process (2) using both the bivariate dependence measure  $\chi_{ij}$  defined in Eq. (1) and the complementary binary measure  $\eta_{ij} := \eta(\mathbf{s}_i, \mathbf{s}_j)$  which is defined by

$$\Pr\{X(\mathbf{s}_i) > F_i^{-1}(u), X(\mathbf{s}_j) > F_j^{-1}(u)\} = \mathcal{L}\{(1-u)^{-1}\}(1-u)^{1/\eta(\mathbf{s}_i, \mathbf{s}_j)}, \quad (9)$$

where  $\mathcal{L}$  is slowly varying at infinity and  $\eta_{ij} \in (0, 1]$  is used to differentiate between the different levels of dependence exhibited by an asymptotically independent pair  $(X_i, X_j)^T$ .

When  $\eta_{ij} = 1$  and  $\mathcal{L} \not\rightarrow 0$ ,  $(X_i, X_j)^T$  is asymptotically dependent, and the remaining cases are all asymptotically independent (Ledford and Tawn, 1996). The value of  $\eta_{ij}$  quantifies the strength of extremal dependence in the upper joint tail when  $\chi_{ij} = 0$ .

**Theorem 2.3.** *Under the assumptions of Proposition 2.1 and 2.2, the process  $\{X(\mathbf{s})\}$  defined in (2) has a nonstationary tail dependence structure. More specifically,*

(a) *If  $\mathcal{C}_i \cap \mathcal{D} = \emptyset$  and  $\mathcal{C}_j \cap \mathcal{D} = \emptyset$ , we have  $\chi(\mathbf{s}_i, \mathbf{s}_j) = 0$  and  $\eta(\mathbf{s}_i, \mathbf{s}_j) = 1/2$ , which corresponds to the near independence case.*

(b) *If  $\mathcal{C}_i \cap \mathcal{D} = \emptyset$  and  $\mathcal{C}_j \cap \mathcal{D} \neq \emptyset$ , we have*

$$\Pr\{X(\mathbf{s}_i) > q_i(t), X(\mathbf{s}_j) > q_j(t)\} \sim c_{ij}t^{-1-1/\alpha}, \text{ as } t \rightarrow \infty,$$

*which gives  $\chi(\mathbf{s}_i, \mathbf{s}_j) = 0$  and  $\eta(\mathbf{s}_i, \mathbf{s}_j) = \frac{\alpha}{\alpha+1} \in (0, \frac{1}{2})$ .*

(c) *If  $\mathcal{C}_i \cap \mathcal{D} \neq \emptyset$  and  $\mathcal{C}_j \cap \mathcal{D} = \emptyset$ , the  $\chi(\mathbf{s}_i, \mathbf{s}_j)$  and  $\eta(\mathbf{s}_i, \mathbf{s}_j)$  values are the same as in (b).*

(d) *If  $\mathcal{C}_i \cap \mathcal{D} \neq \emptyset$  and  $\mathcal{C}_j \cap \mathcal{D} \neq \emptyset$ , we have*

$$t \Pr\{X(\mathbf{s}_i) > q_i(t), X(\mathbf{s}_j) > q_j(t)\} = 2 - d_{ij} - \left( \frac{c_i}{c_i'^{1/\alpha}} + \frac{c_j}{c_j'^{1/\alpha}} \right) t^{1-\frac{1}{\alpha}} - O(t^{2-\frac{2}{\alpha}}),$$

*in which*

$$d_{ij} = \tau^{\frac{\alpha}{\alpha_0}} \sum_{k \in \mathcal{D}} \left( \frac{\omega_{ki}^{1/\alpha}}{c_i'^{1/\alpha}} + \frac{\omega_{kj}^{1/\alpha}}{c_j'^{1/\alpha}} \right)^\alpha \in (1, 2). \quad (10)$$

*The pair  $(X_i, X_j)^T$  is asymptotically dependent with  $\eta(\mathbf{s}_i, \mathbf{s}_j) = 1$  and  $\chi(\mathbf{s}_i, \mathbf{s}_j) = 2 - d_{ij} \in (0, 1)$  when  $\mathcal{C}_i \cap \mathcal{C}_j \neq \emptyset$ , and asymptotically independent with  $\eta(\mathbf{s}_i, \mathbf{s}_j) = \alpha$  when  $\mathcal{C}_i \cap \mathcal{C}_j = \emptyset$ .*

The proof of Theorem 2.3 can be found in Appendix A.4. From this result, we see that long-range asymptotic independence is automatically assured due to the compactness of the basis functions, and local asymptotic dependence is only possible when  $\mathbf{s}_i$  and  $\mathbf{s}_j$  are covered by one same Wendland basis function whose knot is un-tilted (i.e.,  $\theta_k = 0$ ).

Similar to Eq. (5), the sets  $\mathcal{C}_j \cap \mathcal{D}$ ,  $j = 1, \dots, n_s$ , are crucial to the behavior of the so-called exponent function (Huser and Wadsworth, 2020), which is a limiting measure defined by

$$V(x_1, \dots, x_{n_s}) = \lim_{t \rightarrow \infty} t(1 - F[F_1^{-1}\{1 - (tx_1)^{-1}\}, \dots, F_{n_s}^{-1}\{1 - (tx_{n_s})^{-1}\}]).$$

In particular, it is useful to examine the  $n_s$ -dimensional extremal coefficient  $V(1, \dots, 1)$ . This extremal coefficient has a range of  $[1, n_s]$ , with the lower and upper ends indicating, respectively, perfect dependence and independence. As a polarized case, if all  $\theta_k > 0$ ,  $k = 1, \dots, K$ , then  $\mathcal{C}_j \cap \mathcal{D} = \emptyset$  for all  $j$ 's. Thus, we have

$$\theta_k^\alpha - \left\{ \theta_k + \tau^{\frac{1}{\alpha_0}} \sum_{j=1}^{n_s} \frac{\omega_{kj}^{1/\alpha}}{q_j^{1/\alpha_0}(t)} \right\}^\alpha \sim \alpha \tau^{\frac{1}{\alpha_0}} \theta_k^{\alpha-1} \sum_{j=1}^{n_s} \frac{\omega_{kj}^{1/\alpha}}{q_j^{1/\alpha_0}(t)}, \quad u \rightarrow 1.$$

Here, we can approximate  $q_j(t)$  using the results from Corollary 2.1.2. From Eq. (7), we can deduce that  $V(1, \dots, 1) = n_s$ , which corresponds to joint extremal independence. By contrast, if all  $\theta_k = 0$  and one knot covers the entire spatial domain, we have  $V(1, \dots, 1) \in (1, n_s)$  which corresponds to joint extremal dependence.

It is worth noting that the extremal dependence structures in real processes (e.g., hurricanes and thunderstorms) might evolve and change (rapidly) over time. When we try to model many replicates of the process  $\{X_t(\mathbf{s}) : t = 1, \dots, n_t\}$ , it is more physically realistic to have the tilting parameters  $\boldsymbol{\theta} = \{\theta_k : k = 1, \dots, K\}$  vary across time. Therefore, a major advantage of our extVAE introduced in Section 3 is that it permits different  $\boldsymbol{\theta}_t = \{\theta_{kt} : k = 1, \dots, K\}$  at different time  $t$ ,  $t = 1, \dots, n_t$ , which automatically gives us a temporally non-stationary spatial extremes model. To the best of our knowledge, our extVAE is the first attempt to allow spatially and temporally varying extremal dependence structures simultaneously in one model.

### 3 Extreme variational autoencoder

This section provides background on variational autoencoders (VAEs) and describes how we embed the novel spatial extremes model from Section 3 within a VAE.

#### 3.1 Encoding-decoding methods

Principal component analysis (PCA) has been widely used in machine learning for image compression and reconstruction (e.g., [Malagon-Borja and Fuentes, 2009](#)), in neuroscience for spike-triggered covariance analysis (e.g., [Pillow and Simoncelli, 2006](#)) and in atmospheric science for empirical orthogonal function (EOF) analysis (e.g., [Francom et al., 2019](#)). It reduces the dimensionality of a large dataset by encoding high-dimensional features through a linear subspace that spans the highest variance of the data input. Both data compression (or encoding) and data reconstruction (or decoding) in PCA are linear operations on the eigenvectors of the sample covariance matrix. Similarly, an autoencoder also seeks to construct an encoder that reduces the dimensionality and retains the maximum information, and a decoder that reconstructs the data from the encoded space with a minimum error. The main difference with respect to PCA is that an autoencoder sets the encoder and the decoder as neural networks, which are non-linear functions, and learns their best weights and biases by optimizing the loss function iteratively.

However, both PCA and the autoencoders project the data input to a single point in the latent space and they do not allow generation of new content. Moreover, the latent space therein is not regularized in the training process, which suggests that we should not naïvely sample from the latent space and decode the random sample to generate an output realization. By contrast, a variational autoencoder encodes a data input as a latent random variable in the encoded space from which random samples are drawn to be fed into the decoder for generative construction of new output realizations. To regularize the latent space and avoid overfitting, the VAE is trained to maximize the conditional log-likelihood and to minimize the reconstruction loss back-propagated through the network; see [Kingma et al. \(2019\)](#) for a detailed introduction to VAEs.

### 3.2 VAE for spatial data

In the spatial setting, consider a replicate of a process  $\mathbf{X}_t = \{X_t(\mathbf{s}_j) : j = 1, \dots, n_s\}$ , and its encoded  $K$ -dimensional latent random vector  $\mathbf{Z}_t = \{Z_{kt} : k = 1, \dots, K\}$ ,  $t = 1, \dots, n_t$ . The joint model for  $(\mathbf{x}_t, \mathbf{z}_t)$  is parameterized by  $\phi_d$  which includes the weights and biases in the neural network of the decoder, and we denote it by  $p_{\phi_d}(\mathbf{x}_t, \mathbf{z}_t)$ . Then the conditional distributions  $p_{\phi_d}(\mathbf{z}_t | \mathbf{x}_t)$  and  $p_{\phi_d}(\mathbf{x}_t | \mathbf{z}_t)$  are natural choices for encoder and decoder, respectively, but the posterior

$$p_{\phi_d}(\mathbf{z}_t | \mathbf{x}_t) = \frac{p_{\phi_d}(\mathbf{x}_t, \mathbf{z}_t)}{\int p_{\phi_d}(\mathbf{x}_t, \mathbf{z}_t) d\mathbf{z}_t},$$

is often intractable due to the integration in the denominator. A VAE uses a variational-Bayes-based approximation  $q_{\phi_e}(\mathbf{z}_t | \mathbf{x}_t)$ , in which  $\phi_e$  is shared across all replicates (and the method is referred to as amortized variational inference). The marginal distribution of  $\mathbf{X}_t$  can then be rewritten as follows:

$$\begin{aligned} \log p_{\phi_d}(\mathbf{x}_t) &= \int q_{\phi_e}(\mathbf{z}_t | \mathbf{x}_t) \log p_{\phi_d}(\mathbf{x}_t) d\mathbf{z}_t = \int q_{\phi_e}(\mathbf{z}_t | \mathbf{x}_t) \log \frac{p_{\phi_d}(\mathbf{x}_t, \mathbf{z}_t)}{p_{\phi_d}(\mathbf{z}_t | \mathbf{x}_t)} d\mathbf{z}_t \\ &= E_{q_{\phi_e}(\mathbf{z}_t | \mathbf{x}_t)} \left\{ \log \frac{p_{\phi_d}(\mathbf{x}_t, \mathbf{z}_t)}{q_{\phi_e}(\mathbf{z}_t | \mathbf{x}_t)} \right\} + D_{KL} \{q_{\phi_e}(\mathbf{z}_t | \mathbf{x}_t) || p_{\phi_d}(\mathbf{z}_t | \mathbf{x}_t)\}, \end{aligned} \quad (11)$$

in which  $\log p_{\phi_d}(\mathbf{x}_t)$  is also called the *evidence* for  $\mathbf{x}_t$ , and the second term on the right-hand side of (11) is the Kullback–Leibler (KL) divergence between  $q_{\phi_e}(\mathbf{z}_t | \mathbf{x}_t)$  and  $p_{\phi_d}(\mathbf{z}_t | \mathbf{x}_t)$ , which is non-negative. The first term on the right-hand side of (11) is thus called the variational lower bound or evidence lower bound (ELBO):

$$\mathcal{L}_{\phi_e, \phi_d}(\mathbf{x}_t) = E_{q_{\phi_e}(\mathbf{z}_t | \mathbf{x}_t)} \left\{ \log \frac{p_{\phi_d}(\mathbf{x}_t, \mathbf{z}_t)}{q_{\phi_e}(\mathbf{z}_t | \mathbf{x}_t)} \right\},$$

which can be approximated using Monte Carlo as

$$\mathcal{L}_{\phi_e, \phi_d}(\mathbf{x}_t) \approx \frac{1}{L} \sum_{l=1}^L \log \frac{p_{\phi_d}(\mathbf{x}_t, \mathbf{z}^l)}{q_{\phi_e}(\mathbf{z}^l | \mathbf{x}_t)}, \quad (12)$$

where  $\mathbf{z}^1, \dots, \mathbf{z}^L$  are independent draws from  $q_{\phi_e}(\cdot | \mathbf{x}_t)$ .

Eq. (11) implies that maximizing the ELBO is equivalent to maximizing the log-likelihood  $\log p_{\phi_d}(\mathbf{x}_t)$  while minimizing the differences between the approximate  $q_{\phi_e}(\mathbf{z}_t | \mathbf{x}_t)$  and the true  $p_{\phi_d}(\mathbf{z}_t | \mathbf{x}_t)$ . To this end, the VAE employs stochastic gradient search to learn the best encoding-decoding scheme via maximizing  $\sum_{t=1}^{n_t} \mathcal{L}_{\phi_e, \phi_d}(\mathbf{x}_t)$  or the minibatch version of it. Traditionally, the proposal distributions  $q_{\phi_e}(\mathbf{z}_t | \mathbf{x}_t)$  are usually chosen to be normal and the encoder returns the mean and the covariance matrix for these normal distributions. By controlling the mean and variance, the reconstruction error is back-propagated through the Gaussian latent variables and the distributions  $q_{\phi_e}(\mathbf{z}_t | \mathbf{x}_t)$  are enforced to be close to  $p_{\phi_d}(\mathbf{z}_t | \mathbf{x}_t)$ . In addition, the prior  $p_{\phi_d}(\mathbf{z}_t)$  usually follows a simple multivariate normal distribution  $N(\mathbf{0}, I_K)$ , and the data model  $p_{\phi_d}(\mathbf{x}_t | \mathbf{z}_t)$  either has Gaussianity also or does not naturally account for extremal dependence (e.g., Kingma et al., 2019; Cartwright et al., 2023). In the following subsections, we will detail how to combine the max-id process (2) proposed in Section 2 with the VAE.

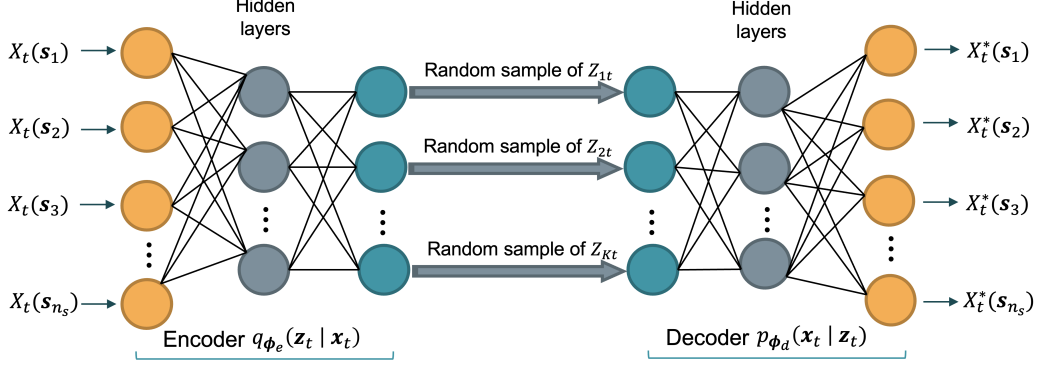


Figure 1: A schematic diagram for the extVAE, in which the parameters  $\phi_e$  and  $\phi_d$  in the encoder  $q_{\phi_e}(\mathbf{z}_t | \mathbf{x}_t)$  and the decoder  $p_{\phi_d}(\mathbf{x}_t | \mathbf{z}_t)$  are both trained using multilayer perceptron (MLP) neural networks, and rectified linear unit (ReLU) is used as activation functions in the hidden layers. In particular, the decoder  $p_{\phi_d}(\mathbf{x}_t | \mathbf{z}_t)$  and the prior  $p_{\phi_d}(\mathbf{z}_t)$  follow the distributional assumptions in Eq. (2)–(4).

### 3.3 Embedding the max-id process in the VAE

For each replicate  $t$ , the hierarchical construction of the process (2) allows us to place the latent exponentially tilted PS variables  $Z_{kt}$ ,  $k = 1, \dots, K$ , in the encoded space of the VAE; that is, we compress/encode the spatio-temporal outputs for the data generating process of interest to the much smaller  $K$ -dimensional latent space, while keeping the distributional assumptions in Eq. (2)–(4) when decompressing/decoding the latent variables back to the initial space. Both the encoder and decoder are multilayer perceptron (MLP) neural networks whose weights are updated iteratively to maximize the differentiable ELBO. See the schematic diagram of our extVAE in Figure 1.

In particular, the parameters in the decoder  $(\alpha_0, \tau, \Omega) \subset \phi_d$  are time-invariant and the dependence parameters  $(\alpha_t, \theta_t)$  are parameterized by  $\phi_d$ :

$$(\alpha_t, \theta_t) = \text{DecoderNeuralNet}_{\phi_d}(\mathbf{z}_t); \quad (13)$$

see Eq. (22) and (23) in Appendix C.1 for more details. From Eq. (3), we know that

$$\Pr(\mathbf{X}_t \leq \mathbf{x}_t | \mathbf{Z}_t, \phi_d) = \exp \left\{ - \sum_{j=1}^{n_s} \left( \frac{\tau}{x_{jt}} \right)^{\frac{1}{\alpha_0}} \sum_{k=1}^K \omega_{kj}^{\frac{1}{\alpha}} Z_{kt} \right\}.$$

Differentiating the conditional distribution function gives the exact form of the decoder:

$$p_{\phi_d}(\mathbf{x}_t | \mathbf{z}_t) = \left( \frac{1}{\alpha_0} \right)^{n_s} \left\{ \prod_{j=1}^{n_s} \frac{1}{x_{jt}} \left( \frac{x_{jt}}{\tau y_{jt}} \right)^{-1/\alpha_0} \right\} \exp \left\{ - \sum_{j=1}^{n_s} \left( \frac{x_{jt}}{\tau y_{jt}} \right)^{-1/\alpha_0} \right\},$$

in which  $y_{jt} = \sum_{k=1}^K \omega_{kj}^{1/\alpha} z_{kt}$ . Denoting the density function of Eq. (4) by  $H(z; \alpha, \alpha, \theta_k)$  (see Appendix A.1 for its expression), the prior on  $\mathbf{z}_t$  can be written as

$$p_{\phi_d}(\mathbf{z}_t) = \prod_{k=1}^K H(z_{kt}; \alpha, \alpha, \theta_{kt}). \quad (14)$$

For the encoder, we compress the each observed spatial replicate  $\mathbf{x}_t$ ,  $t = 1, \dots, n_t$ , and construct the latent distributions for  $q_{\phi_e}(\mathbf{z}_t \mid \mathbf{x}_t)$  using the reparameterization trick (see Section 2.4 in [Kingma et al., 2019](#), for details) with an auxiliary variable  $\boldsymbol{\eta}_t$ :

$$\begin{aligned} (\boldsymbol{\mu}_t, \log \boldsymbol{\sigma}_t) &= \text{EncoderNeuralNet}_{\phi_e}(\mathbf{x}_t), \\ \eta_{kt} &\stackrel{\text{i.i.d.}}{\sim} \text{HalfNormal}(0, 1), \\ \mathbf{z}_t &= \boldsymbol{\mu}_t + \boldsymbol{\sigma}_t \odot \boldsymbol{\eta}_t, \end{aligned} \tag{15}$$

in which  $\boldsymbol{\eta}_t = \{\eta_{kt} : k = 1, \dots, K\}$  and  $\odot$  is the elementwise product.

### 3.4 ELBO and stochastic gradient descent optimization

From Eq. (12), the ELBO can be approximated by:

$$\mathcal{L}_{\phi_e, \phi_d}(\mathbf{x}_t) = \frac{1}{L} \sum_{l=1}^L \{ \log p_{\phi_d}(\mathbf{x}_t \mid \mathbf{z}^l) + \log p_{\phi_d}(\mathbf{z}^l) - \log q_{\phi_e}(\mathbf{z}^l \mid \mathbf{x}_t) \},$$

in which the forms of the decoder and encoder are defined in Eq. (13)–(15); see Appendix C.1 for the exact expression of the ELBO, for which we followed the Monte Carlo integration steps in Appendix 4 of [Bopp et al. \(2021\)](#) to calculate the log-prior,  $\log H(z; \alpha, \alpha, \theta_k)$ .

A major advantage of formulating the ELBO is that it allows joint optimization over all parameters ( $\phi_e$  and  $\phi_d$ ) using stochastic gradient descent (SGD), which is implemented with the help of a tape-based automatic differentiation module called `autograd` in the R package `torch` ([Falbel and Luraschi, 2023](#)). This package is based on PyTorch which provides fast array computation with strong GPU acceleration. It stores all the data inputs and VAE parameters in forms of `torch` tensors, which are similar to R multi-dimensional arrays but are designated for fast and scalable mathematical calculations as well as differentiation.

Algorithm 1 outlines the pseudo algorithm for the ELBO optimization of our extVAE. As the ELBO is constructed within each iteration of the SGD algorithm, the `autograd` module of `torch` tracks the computations (i.e., linear operations and ReLU activations on the tensors) in all layers of the encoding/decoding neural networks, and then performs the reverse-mode automatic differentiation via a backward pass through the graph of tensor operations to obtain the partial derivatives or the gradients with respect to each weight and bias parameter ([Keydana, 2023](#)). Algorithm 1 then takes repeated steps in the direction of the gradients (i.e., direction of the steepest ascent on the ELBO curve) coupled with a learning rate  $\nu > 0$  dictating how big of a step to take.

Additionally, we tried momentum ([Polyak, 1964](#)), RMSProp ([Tieleman et al., 2012](#)) and Adam ([Kingma and Ba, 2014](#)) in our experiments to adapt the learning rate and to speed up the convergence in the SGD algorithm. The momentum approach works best for our model. Moreover, we found that the number of Monte Carlo samples  $L$  can be set to 1 as long as the minibatch size  $|\mathcal{M}|$  is sufficiently large, which was also recommended in [Kingma and Welling \(2013\)](#). We start with initial learning rate  $\nu = 10^{-12}$  and slowly increase it along with the training process, as the training process is not able to handle relatively



---

**Algorithm 1** Stochastic Gradient Descent with momentum to maximize the ELBO defined in Eq. (12). We set  $|\mathcal{M}| = n_t$  and  $L = 1$  in our experiments.

---

**Input:** Learning rate  $\nu$ , momentum parameter  $\zeta$ , convergence tolerance  $\delta$

$\{\mathbf{x}_t : t = 1, \dots, n_t\}$ : observed  $n_t$  spatial replicates

$q_{\phi_e}(\mathbf{z}_t | \mathbf{x}_t)$ : Inference model

$p_{\phi_d}(\mathbf{x}_t, \mathbf{z}_t)$ : Generative data model

**Result:**

$\phi_e, \phi_d$ : Optimized parameters

$j \leftarrow 0$ ;

$K \leftarrow$  Number of data-driven knots;

$\{\tilde{\mathbf{s}}_1, \dots, \tilde{\mathbf{s}}_K\} \leftarrow$  Coordinates of the knots;

$r \leftarrow$  Wendland basis radius shared by all knots; // See Section 5.1 for details

$(\phi_e^{(j)}, \phi_d^{(j)})^T \leftarrow$  Initialized parameters; // See Appendix C.2 for details

$\mathbf{v} \leftarrow \mathbf{0}$ ; // Velocity

$\mathbf{L} \leftarrow \text{repeat}(-\text{Inf}, 200)$ ; // A vector of 200 negative infinite values

**while**  $|\text{mean}\{\mathbf{L}[(j-200):(j-101)]\} - \text{mean}\{\mathbf{L}[(j-100):j]\}| > \delta$  **do**

$\mathcal{M} \sim \{1, \dots, n_t\}$ ; // Indices for the random minibatch

$\eta_{kt} \stackrel{\text{i.i.d.}}{\sim} \text{HalfNormal}(0, 1)$ ,  $k = 1, \dots, K$ ,  $t \in \mathcal{M}$ ; // Reparameterization trick

**for**  $t \in \mathcal{M}$  **do**

$(\boldsymbol{\mu}_t, \log \boldsymbol{\sigma}_t) \leftarrow \text{EncoderNeuralNet}_{\phi_e^{(j)}}(\mathbf{x}_t)$ ;

$\mathbf{z}_t \leftarrow \boldsymbol{\mu}_t + \boldsymbol{\sigma}_t \odot \boldsymbol{\eta}_t$ ;

$(\alpha_t, \boldsymbol{\theta}_t) \leftarrow \text{DecoderNeuralNet}_{\phi_d^{(j)}}(\mathbf{z}_t)$ ;

        Calculate  $q_{\phi_e^{(j)}}(\mathbf{z}_t | \mathbf{x}_t)$ ,  $p_{\phi_d^{(j)}}(\mathbf{x}_t | \mathbf{z}_t)$  and  $p_{\phi_d^{(j)}}(\mathbf{z}_t)$ ; // See Eq. (13)-(15)

**end**

    Obtain the ELBO  $\mathcal{L}_{\phi_e^{(j)}, \phi_d^{(j)}}(\mathcal{M}) = \sum_{t \in \mathcal{M}} \mathcal{L}_{\phi_e^{(j)}, \phi_d^{(j)}}(\mathbf{x}_t)$  and its gradients  $\mathbf{J}_{\mathcal{L}} =$

$\{\nabla_{\phi_e, \phi_d} \mathcal{L}_{\phi_e, \phi_d}(\mathcal{M})\}(\phi_e^{(j)}, \phi_d^{(j)})$ ;

    Compute velocity update:  $\mathbf{v} \leftarrow \zeta \mathbf{v} + \nu \mathbf{J}_{\mathcal{L}}$ ;

    Apply update:  $(\phi_e^{(j+1)}, \phi_d^{(j+1)})^T \leftarrow (\phi_e^{(j)}, \phi_d^{(j)})^T + \mathbf{v}$ ;

$\mathbf{L} \leftarrow (\mathbf{L}^T, \mathcal{L}_{\phi_e^{(j)}, \phi_d^{(j)}}(\mathcal{M}))^T$ ; // Add the latest ELBO value to the vector  $\mathbf{L}$

$j \leftarrow j + 1$ ;

**end**

---

large learning rates at initial steps. After we have trained the model parameters  $\phi_e$  and  $\phi_d$ , we can efficiently run the encoder and decoder as many times as needed to produce an ensemble of numerous different samples that all come from the same distribution as the spatial inputs.

More importantly, our extVAE algorithm can be efficiently scaled to large spatial data sets. It is currently not possible to fit existing max-stable, inverted-max-stable, and other spatial extremes models using a full likelihood or Bayesian approach on a dataset of more than 1000 locations. Richards et al. (2023) used likelihood-free inference with neural Bayes estimators to fit the Huser and Wadsworth (2020) model on a space-time dataset com-

parable in size to our Red Sea surface temperature data in Section 6, but they split the spatial domain into moving windows, each of which contains  $16 \times 16$  grid points. As a result, their estimated parameters from each local window that determines the extremal dependence structure can only reveal the dependence properties locally, and the disjoint analyses on the subsets of the data were not integrated together and hence global conclusions on the joint tail decay for two locations in different moving windows cannot be drawn. By contrast, [Sainsbury-Dale et al. \(2022b\)](#) analyzed the entire spatial domain using the single-station conditional model ([Wadsworth and Tawn, 2022](#)), but it can only exhibit one dependence class and the user has to specify a conditioning site.

## 4 Model evaluation approaches

### 4.1 Proper scoring rules

To interpolate at the 100 holdout locations  $\{\mathbf{g}_i : i = 1, \dots, 100\}$ , we only need to calculate the Wendland basis function values at the these locations, with which we can mix the encoded variables from Eq. (15) to get the predicted values. For each time  $t$  and holdout location  $\mathbf{g}_i$ , denote the true observation of  $Y_t(\mathbf{g}_i)$  by  $y_{it}$  and the emulated prediction by  $y_{it}^*$ . Then the mean squared prediction error (MSPE) for time  $t$  is

$$\text{MSPE}_t = \frac{1}{100} \sum_{i=1}^{100} (y_{it} - y_{it}^*)^2,$$

in which  $t = 1, \dots, n_t$ . All MSPEs from different time replicates can be summarized in a box plot; see Figure 3d for example. Similarly, we calculate the continuously ranked probability score (CRPS; [Matheson and Winkler, 1976](#)) across time for each location

$$\text{CRPS}_i = \frac{1}{n_t} \sum_{t=1}^{n_t} \int_{-\infty}^{\infty} (F_i(z) - \mathbb{1}(y_{it}^* \leq z))^2 dz,$$

where  $F_i$  is the marginal distribution estimated using parameters at the holdout location  $\mathbf{g}_i$ ,  $i = 1, \dots, 100$ , and again  $y_{it}^*$  is the emulated value. Smaller CRPS indicates that the distribution  $F_{Y_i}$  is concentrated around  $y$ , and thus can be used to measure how well the distribution fits all emulated values. Figure 3d also shows how we present the CRPS values from all holdout locations for each emulation.

### 4.2 Dependence structures

The  $\chi_{12}(u)$  formula defined by Eq. (1) is a bivariate measure that may have different shapes as we move the pair across the domain when the process  $\{X(\mathbf{s}) : \mathbf{s} \in \mathcal{S}\}$  is non-stationary. Nevertheless, in this subsection we treat  $\{X(\mathbf{s}) : \mathbf{s} \in \mathcal{S}\}$  defined in Eq. (2) as if it has a stationary and isotropic dependence structure so that  $\chi_{12}(u) \equiv \chi_h(u)$ . This surely violates our model assumption but it is still a useful way of summarizing the dependence properties at different distances  $h$  and different quantile levels  $u$ . Compared to QQ-plot which also

can be used to check two data sets to see if they come from populations with a common distribution,  $\chi_h(u)$  can isolate the dependence in the tail at a fixed distance  $h$ .

The nonparametric estimator of  $\chi_h(u)$  described below is similar to an empirical variogram estimator (see Figure 4 in Zhang et al., 2022b). For a fixed  $h$ , we find all pairs of locations with similar distances (within a small tolerance  $\epsilon = 0.001$ ), and compute the empirical conditional probabilities  $\hat{\chi}_h(u)$  at a grid of  $u$  values. The confidence envelopes are calculated by regarding the outcome (i.e., simultaneously exceed  $u$  or not) of each pair as a Bernoulli variable and computing pointwise binomial confidence intervals, assuming that each pair of points is independent from each other. Figure 7 demonstrates how this empirical measure can be useful in comparing the extremal dependence structures between the spatial data input and its emulations.

To avoid the stationarity assumption, we can also estimate the pairwise  $\chi$  measure when there are sufficient time replicates. Choose a reference point denoted by  $\mathbf{s}_0$ , we can estimate the pairwise  $\chi_{\mathbf{s}_0, \mathbf{s}}(u)$  empirically for any  $\mathbf{s}$  in the spatial domain  $\mathcal{S}$  only using the values from these two locations. Figure 13 shows a raster plot of the empirical  $\chi_{\mathbf{s}_0, \mathbf{s}}(u)$ ,  $u = 0.85$ , estimated from the Red Sea surface temperature data set, in which  $\mathbf{s}_0$  is the center of the spatial domain and  $\mathbf{s}$  is an element of uniform grid.

### 4.3 Average radius of exceedance

Although useful, the dependence measure  $\chi_h(u)$  is very restrictive in that it requires stationarity and isotropy, and it only examines pairwise dependence at a fixed distance. To avoid making assumptions about the second-order trend and only focus on the length scales of the extreme events (e.g., “storms”) or peaks-over-threshold, Zhang et al. (2022a) developed a metric called the averaged radius of exceedance (ARE) that characterizes the spatial structure of extreme events conditional on the fact that an arbitrary reference point in the domain (e.g., the center of the spatial domain) exceeds a particular quantile  $u$ .

The ARE is calculated as follows: first, under one of the true Models I–IV, we simulate 20,000 replicates from the process on a  $0.1 \times 0.1$  grid over the square  $[0, 10] \times [0, 10]$ . Then we transform them into uniform scales using the empirical marginal distribution functions, and keep replicates in which the reference point exceeds a specific high quantile level  $u$ . For each retained replicate, we count the grid cells that exceed  $u$  at the same time (denoted this number by  $N_e(u)$ ), and sum over the area of all grid cells via the formula  $A_{\text{tot}}(u) = 0.1^2 \times N_e(u)$ . Then, the averaged radius of exceedance (ARE) can be approximated by  $\{A_{\text{tot}}(u)/\pi\}^{-1/2} \equiv \text{ARE}(u)$ . We repeat this calculation for each replicate and obtain many estimated radii of exceedance and take the average over all replicates to obtain the best estimates of  $\text{ARE}(u)$  and its confidence envelopes. By analogy, we can evaluate  $\text{ARE}(u)$  for the emulators via generating many replicates of the process on the same grid. Since the ARE metric is dependent on which reference point we choose, it does not require stationarity or isotropy, and only quantifies the spatial extent of simultaneous occurrences given that one location reaches a certain level of extremeness. Figure 9 displays the estimates of  $\text{ARE}(u)$  for different spatial data inputs and their extVAE emulations.

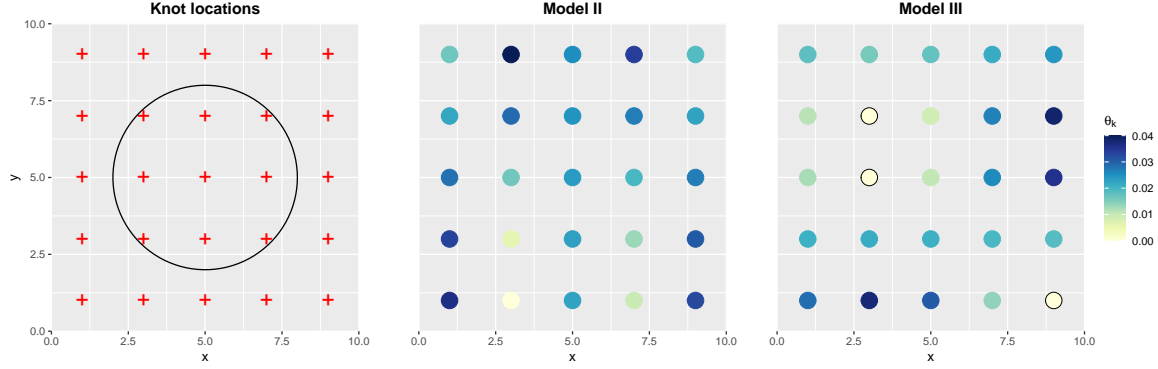


Figure 2: The left panel presents knot locations used for simulating data under Models II–IV, and we only show the support of the one Wendland basis function centered at knot in the middle of the domain. Model V uses the same set of knots but the basis function is not compactly supported. The middle and right panels display the  $\theta_k$  values,  $k = 1, \dots, K$ , used in the exponentially-tilted PS variables at each knot for Models II and III respectively; see Eq. (4). The circled knots signify  $\theta_k = 0$ , which induces local asymptotic dependence.

## 5 Simulation study

To assess the performance of our flexible spatial extremes model, we conduct a simulation study which contains  $n_s = 2000$  locations randomly sampled from the uniform distribution on the square  $[0, 10] \times [0, 10]$ . We simulate  $n_t = 100$  replicates from each of the following three different models:

- I. Gaussian process with zero mean and Matérn covariogram  $C(\mathbf{s}_j, \mathbf{s}_j; \phi, \nu)$ , in which  $\phi = 3$  and  $\nu = 5/2$ ;
- II. Max-id process (2) with  $K = 25$  and  $|\mathcal{D}| = 0$ ;
- III. Max-id process (2) with  $K = 25$  and  $0 < |\mathcal{D}| < K$ ;
- IV. Max-id process (2) with  $K = 25$  and  $|\mathcal{D}| = K$ ;
- V. Max-stable Reich and Shaby (2012) model with  $K = 25$ .

Models I–V gradually exhibit more and more extremal dependence, and they can help us test whether the extVAE can capture spatially-varying dependence structures that exhibit local asymptotic dependence and/or local asymptotic independence. Since the max-id process (2) allows the dependence parameter  $\theta_k$  to change at different knots ( $k = 1, \dots, K$ ), a well-trained extVAE should be able to differentiate between local asymptotic dependence ( $\theta_k = 0$ ) and local asymptotic independence ( $\theta_k > 0$ ).

Model I is a stationary and isotropic Gaussian process with a Matérn covariance function. It is known that the joint distribution of the Gaussian process at any two locations  $\mathbf{s}_i$  and  $\mathbf{s}_j$  is light-tailed and thus leads to asymptotic independence unless the correlation  $\rho(\mathbf{s}_i, \mathbf{s}_j) = 1$ . For Models II, III and IV, we simulate data from the max-id model (2) with  $K = 25$  knots evenly across the grid and denote them by  $\{\tilde{\mathbf{s}}_1, \dots, \tilde{\mathbf{s}}_K\}$ . Setting  $r = 3$ ,

we use the compactly supported Wendland basis function  $\omega_k(\mathbf{s}, r) = \{1 - d(\mathbf{s}, \tilde{\mathbf{s}}_k)/r\}_+^2$  centered at each knot (Wendland, 1995),  $k = 1, \dots, K$ ; see Figure 2. The basis values are standardized so that for each  $\mathbf{s}$ ,  $\sum_{k=1}^K \omega_k(\mathbf{s}, r) = 1$ . The main difference between Models II, III and IV lies in the  $\theta_k$  values — Model II has no zero  $\theta_k$ ’s (i.e.,  $|\mathcal{D}| = 0$ ), whereas Model III has a mix of positive and zero  $\theta_k$ ’s, and Model IV only has zero  $\theta_k$ ’s (i.e.,  $|\mathcal{D}| = K$ ). By Theorem 2.3, we know Model II gives only local asymptotic independence and Model IV gives only local asymptotic dependence. In contrast, Model III gives both local asymptotic dependence and local asymptotic independence. Moreover, Model V adopts the same set of knots but it uses Gaussian radial basis functions which are not compactly supported. Therefore, Model V belongs to the class of Max-stable Reich and Shaby (2012) models, and has stronger extremal dependence than Model IV.

When simulating from Models II–V, we need to sample from the exponentially-tilted PS distributions defined in Eq. (4) for each time replicate. Instead of using the double rejection sampler in Devroye (2009), we adopt the simple rejection sampler described in Section 3 of the Supplement Materials in Bopp et al. (2021) for sampling  $Z_{kt}$ . The double rejection sampler is harder and slower to implement but it is very useful when the tilting parameter is large. However, the  $\theta_k$  in Model II and III are relatively small so we chose the simple rejection sampler. Additionally for Models II–V, the white noise process  $\epsilon_t(\mathbf{s})$  follows the same independent Fréchet(0,  $\tau$ ,  $1/\alpha_0$ ) distribution with  $\tau = 1$  and  $\alpha_0 = 1/4$ .

For each space-time simulated data set, we randomly hold out 100 locations as a validation set. We emulate the data input and characterize the dependence structure at the remaining 1,900 locations using both the proposed extVAE and a Gaussian process regression with heteroskedastic noise implemented in the R package `hetGP` (Binois and Gramacy, 2021). In the following results sections, we show that all emulators will have good performances when emulating data sets from Models I and II, but `hetGP` fails to capture the asymptotic dependence in Models III–V.

## 5.1 Effect of knot locations

For Models II–V, the true knot locations are known, which is usually not the case in a real-world application. In this subsection, we compare the emulation performance when we initialize the extVAE using the true knots/radii and data-driven knots/radii. The idea is that the variational autoencoder will adapt and traverse the parameter space to learn the best weights even when the number of knots  $K$  (i.e., the dimension of the encoded space) is misspecified and different from the truth.

For the data-driven case, we facilitate the convergence of the stochastic gradient search algorithm by finding good initial values for the weights. First, we perform  $k$ -means clustering on each time replicate of the data input on the uniform scales to determine how many clusters of high values ( $u > 0.95$ ) there are, and train extVAE with  $K$  being the number of clusters combined for all time replicates. Second, the cluster centroids are used as knot locations  $\{\tilde{\mathbf{s}}_1, \dots, \tilde{\mathbf{s}}_K\}$ . To initialize  $\boldsymbol{\Omega}$  using the Wendland basis functions  $\omega_k(\mathbf{s}, r) = \{1 - d(\mathbf{s}, \tilde{\mathbf{s}}_k)/r\}_+^2$ ,  $k = 1, \dots, K$ , we pick  $r$  by looping over clusters and calculating the Euclidean distance of each point within one cluster from its centroid, and we set the maximum of all distances as the initial  $r$ . If  $r$  is not large enough for all  $\omega_k(\mathbf{s}, r)$

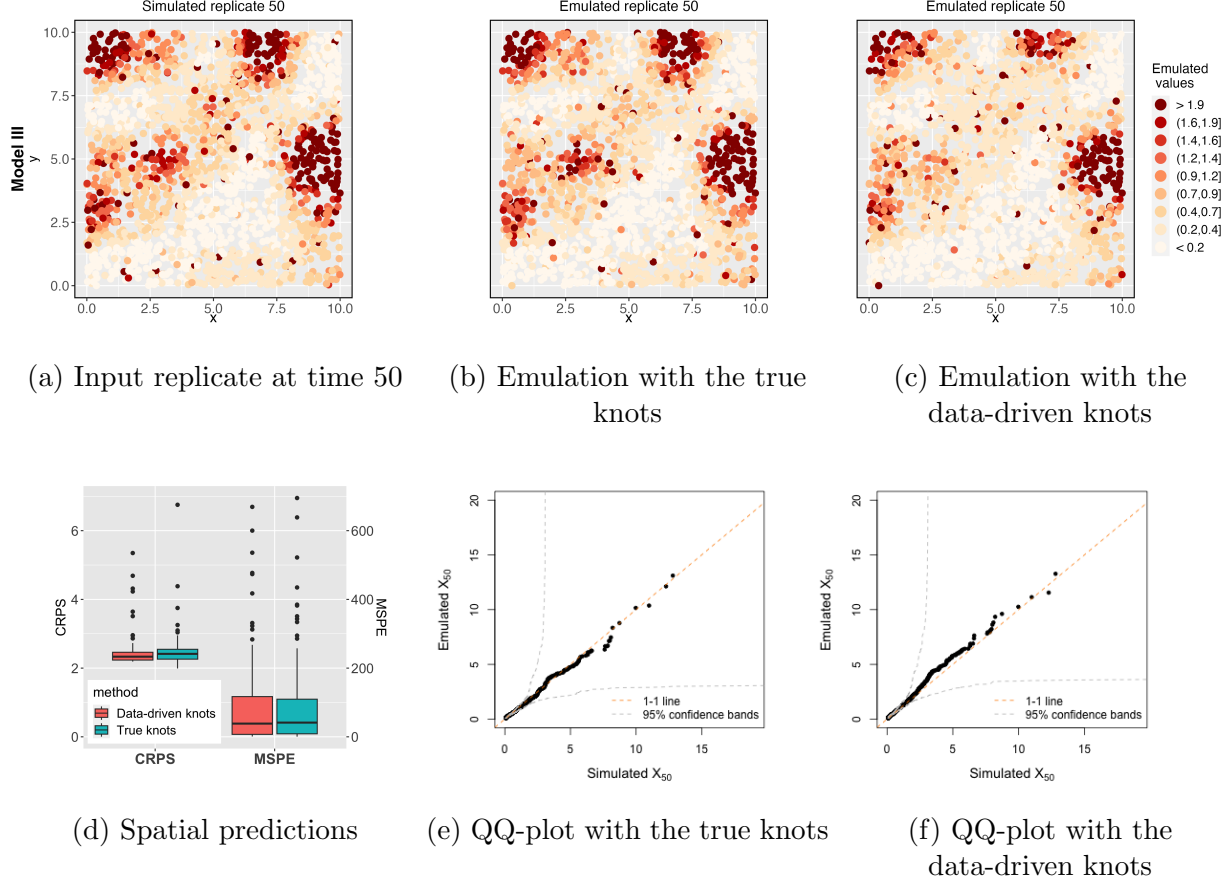


Figure 3: Comparing the emulation results from initializing the extVAE with the true knots and data-driven knots for data simulated from Model III.

to cover the entire spatial domain, we gradually increase  $r$  until the full coverage is met. More details on finding good initial values for  $(\phi_e, \phi_d)$  are deferred to Appendix C.2.

Figure 3 displays the results from emulating the data set simulated from Model III while initializing the weights differently using the true knots and the data-driven knots. Figure 3b and 3c shows one emulation replicate from the decoder for the first time replicate. We see that both figures bear striking resemblance to the original simulation, and from visual examination, we can see little difference in the quality of the emulations. Figure 3d compares the spatial predictions on the 100 holdout locations from the two emulations. We see that emulation with true knots yields slightly better CRPS and MSPE than emulation with data-driven knots, but the spread of the boxplots is quite similar.

Figures 3e and 3f compares the simulated and emulated spatial fields of the 50th replicate by plotting their quantiles against each other. We see that both emulations align very well with the simulated data set. Although this might not be the most appropriate way of evaluating the quality of the emulations because there is no spatial dependence and non-stationarity within each spatial replicate, QQ-plots still provide value in determining whether the spatial distributions are similar at all quantile levels, which is complementary



to the empirical  $\chi(u)$  estimated we described earlier in Section 4.2.

Overall, Figure 3 demonstrates that the data-driven knots perform similarly to the true knots. This justifies applying the extVAE on a data set from a misspecified model (i.e., Models I or V) for which the data-generating process does not involve any Wendland basis functions. Thus, we will use data-driven knots in all applications of the remaining simulation studies and the real data analysis.

## 5.2 Emulation results

Figures 4 and 5 compare the emulated replicates from the extVAE and **hetGP** with the simulated replicates from Models I–V. We see that for the Gaussian process simulated from Model I, both emulators produce similar spatial fields and the QQ-plots all align well with the 1-1 line. Recall the tilting parameters  $\theta_t$  control the local dependence properties. Since the Gaussian process has fairly weak extremal dependence, the resulting  $\theta_t$  estimated in (13) after convergence is consistently greater than 0.1, indicating light tails in the exponentially tilted PS variables and thus, local asymptotic independence at all knots. Similarly for Model II, there is asymptotic independence everywhere in the domain. However, the  $\theta_k$  values we used for Model II are much smaller than 0.1 (see Figure 2) and thus the fitted exponentially tilted PS variables are more heavy-tailed than the ones from the previous case. Therefore, we can see that **hetGP** has difficulty in capturing the extremal dependence and the QQ-plot shows that the tail is underestimated, even though Model II still exhibits asymptotic independence only.

For Models III – V, there is local asymptotic dependence, and we see that **hetGP** completely failed to emulate the co-occurrences of the extreme values. Because **hetGP** focuses on the bulk of the distributions, they tend to ignore the spatial autocorrelation at the tail (especially when  $u > 0.95$ ; see also Figure 7). This validates the need to incorporate a flexible copula model in the emulator to characterize the tail dependence accurately.

Figure 6 compares the performance of spatial predictions at the 100 holdout locations. For Model I, **hetGP** had lower CRPS and MSPE scores, indicating higher predictive power, as expected since the true process was a Gaussian process. However, the extVAE model still performs well in this case. For all the other models, extVAE uniformly outperforms **hetGP**. For models IV and V, the marginal distributions are more heavy-tailed over the spatial domain, and the CRPS and MSPE consistently have larger values than other models. Note that the CRPS and MSPE for **hetGP** can get extremely high for time replicates with extreme events.

Figure 7 compares the nonparametric estimates of the upper tail dependence  $\chi_h(u)$  between simulations and emulations at three difference distances  $h = 0.5, 2, 5$ . In general, we see that the dependence strength decays as  $h$  or  $u$  increases. The results in Figure 7 demonstrate that our extVAE managed to accurately emulate the dependence at both low and high quantiles and empirical confidence envelopes of  $\chi_h(u)$  are indistinguishable between the simulation and emulation.

Figure 8 demonstrates the inferential power of the extVAE to estimate  $\theta = \{\theta_k : k = 1, \dots, K\}$  and correctly categorize the extremal dependence class, which encourages the users to also use the extVAE as an inference tool for the max-id process (2). Given that



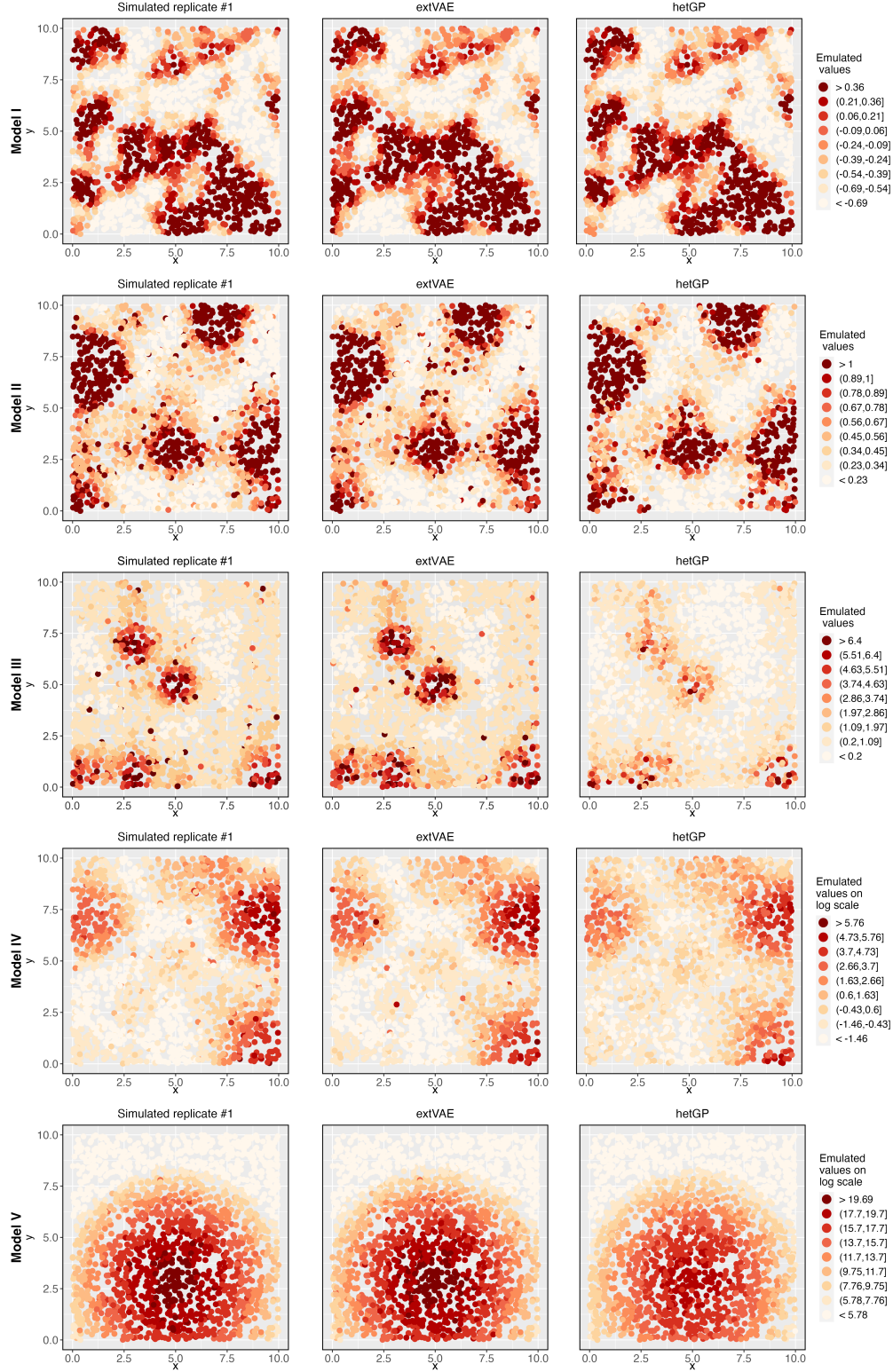


Figure 4: Simulated data sets (left column) and emulated fields (right two columns: extVAE - middle column; hetGP - right column) from Models I–V. In all cases, we use data-driven knots for emulation using extVAE.

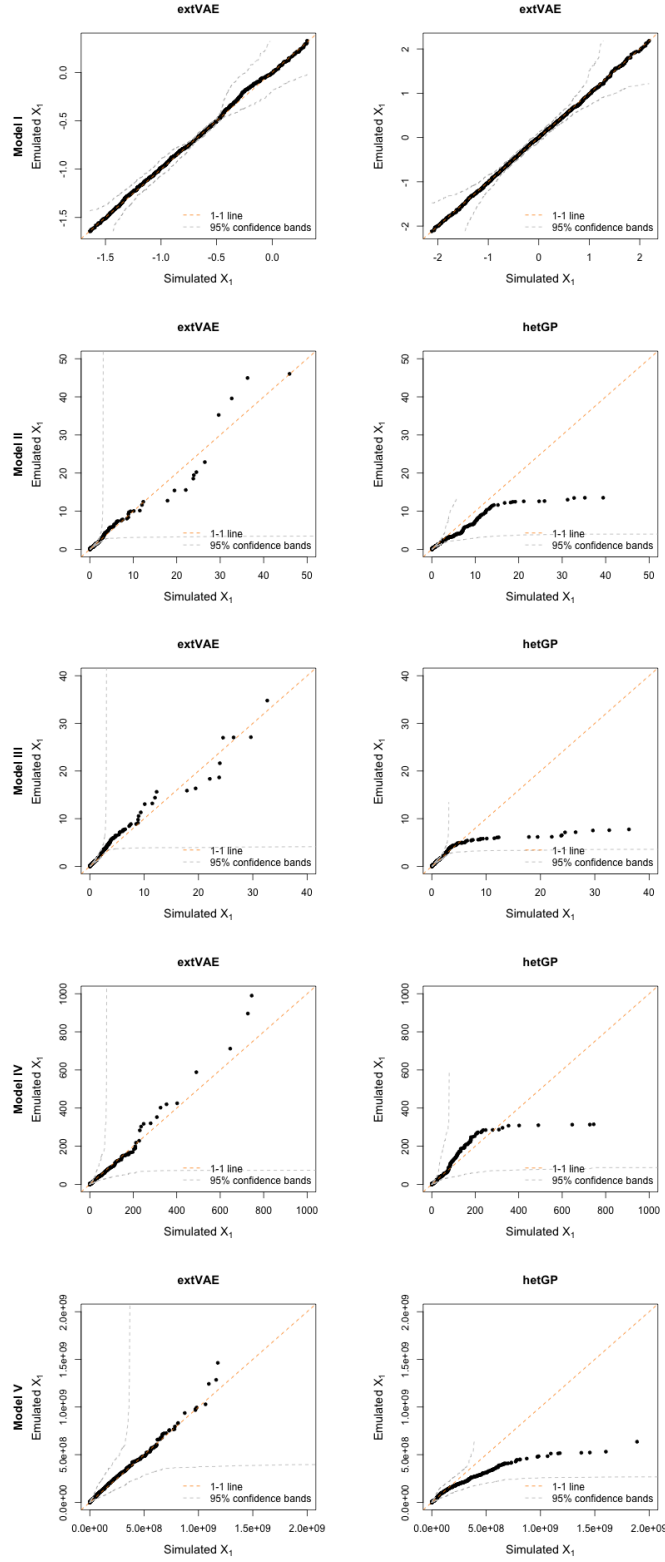


Figure 5: QQ-plots comparing simulated data sets and emulated fields from extVAE (left), and hetGP (right).

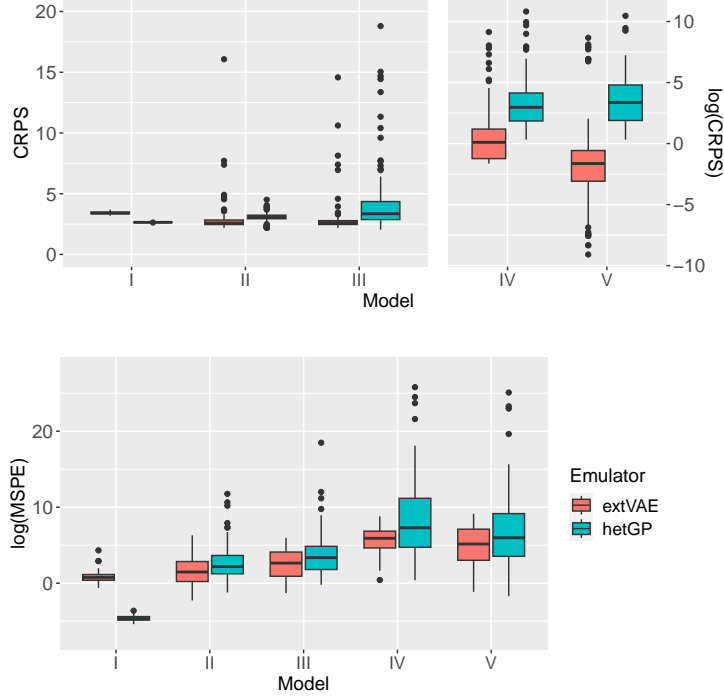


Figure 6: The CRPS and MSPE values from two emulation approaches on the data sets simulated from Models I–V. For both metrics, lower values indicate better emulation results. Also, for Models IV and V, we plot the CRPS values on the log scale since the AD in the data generating process causes the margins to be very heavy-tailed.

Theorem 2.3 ensures highly flexible dependence properties for the process (2), modeling spatial extremes with our extVAE will give a more accurate view of the length scales (see Section 4.3 for more illustrations) and dependence strengths of the extreme events. Moreover, Figure 8 shows that our extVAE framework allows for uncertainty quantification within a Bayesian framework.

Choosing the center of domain (5, 5) as the reference point, Figure 9 displays the estimates of  $\text{ARE}(u)$  for both simulations and emulations under Models I–IV. We see that the empirical AREs from the extVAE are consistent with the ones estimated from the data except for Model V, where the length scale  $\text{ARE}(u)$  is underestimated at low  $u$ 's but overestimated for high  $u$ 's. As expected, the limit of ARE as  $u \rightarrow 1$  is non-negative for Models III–V when there is local asymptotic dependence, and the limit increases as the dependence strength becomes stronger.

## 6 Red Sea surface temperature analysis

In our real-world application, we analyze and emulate a Red Sea surface temperature dataset, which consists of satellite-derived daily sea surface temperature (SST) estimates in Celsius ( $^{\circ}\text{C}$ ) at 16,703 locations on a  $1/20^{\circ}$  grid from 1985/01/01 to 2015/12/31 (11,315

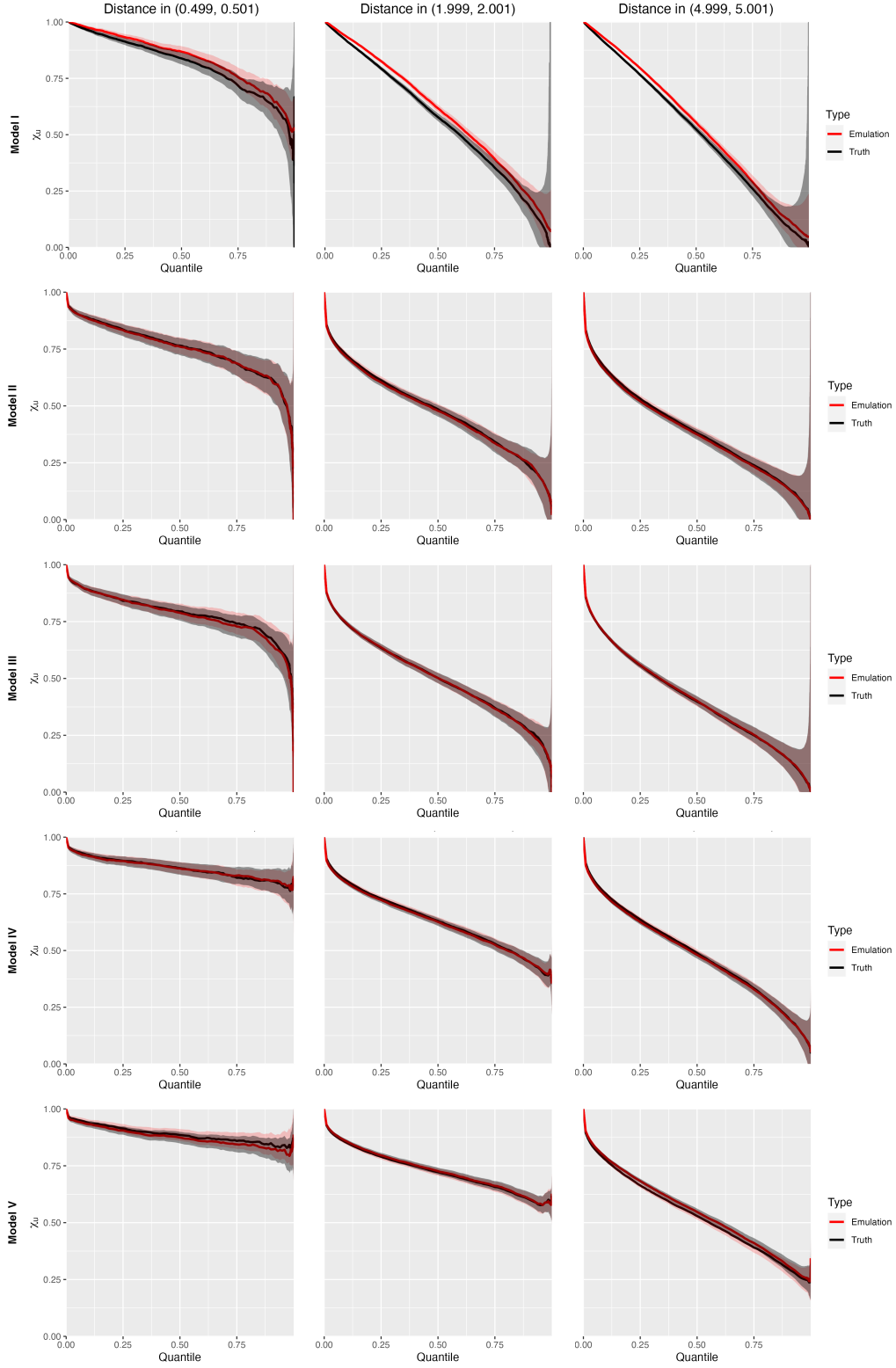


Figure 7: The empirically-estimated tail dependence measure  $\chi_h(u)$  at  $h = 0.5$  (left), 2 (middle), 5 (right) for Models I–V.

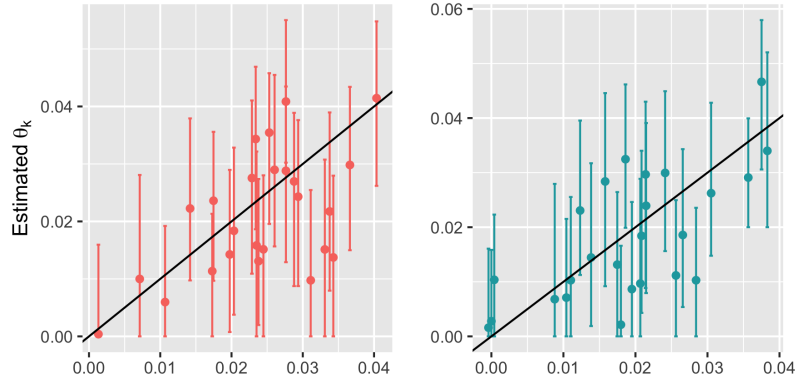


Figure 8: Initializing the extVAE using the true knots from Models II and III, we show the medians and 2.5% and 97.5% quantiles of the  $n_t$  estimates of  $\theta_k$ ,  $k = 1, \dots, K$ , from the decoder (13). The black line is the 1-1 line for reference.

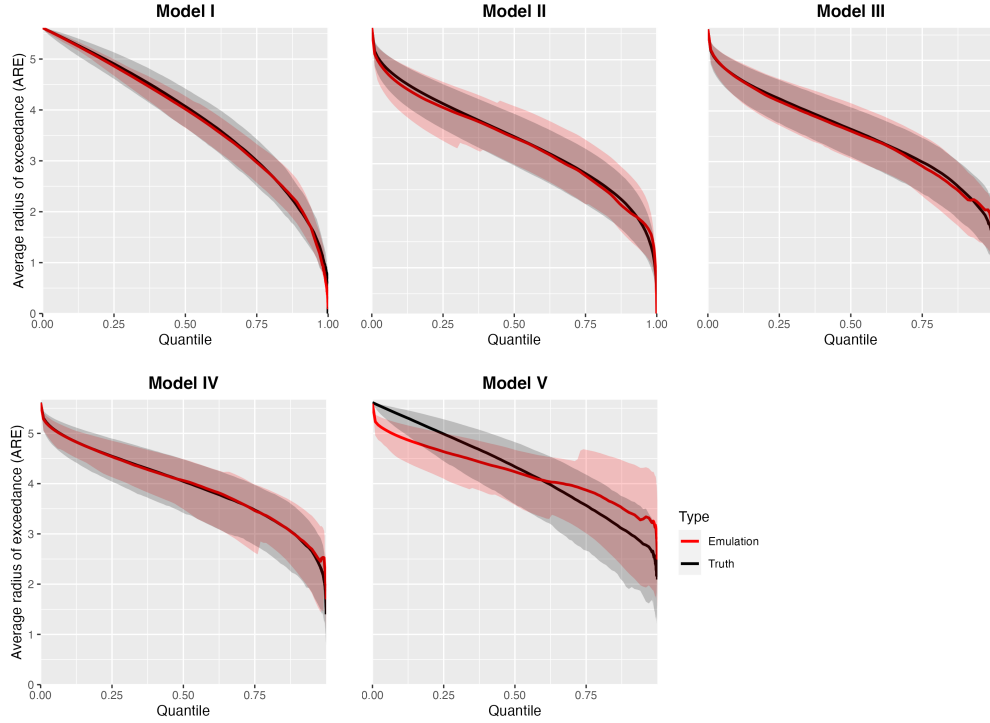


Figure 9: The estimates of  $\text{ARE}(u)$  for both simulations and extVAE emulations under Models I–V.

days in total). This dataset has previously been analyzed in Hazra and Huser (2021), Simpson et al. (2020), Simpson and Wadsworth (2021) and Sainsbury-Dale et al. (2022b). The latter three studies only focused on a small portion of the Red Sea and only the summer months to eliminate the effects of seasonality. For example, Sainsbury-Dale et al. (2022b) retained a data set with only 678 spatial locations and 141 replicates. Hazra and Huser (2021) extensively studied the entire spatial domain using a Dirichlet process mixture (DPM) of low-rank spatial Student’s  $t$  processes (LTPs) to account for the second-order spatial dependence. However, their model is asymptotically dependent for any pair of locations, and the computational time for the final best LTP-DPM model is about 10 hours, while it is about 4.5 hours for our extVAE training and generating emulated replicates.

Since the daily SST at each location exhibits a clear trend and seasonality across seasons and years and the temporal dependence strengths vary at different locations, we first detrend and remove the seasonality before extracting the block maxima and applying our model. Following Section 3.2 of Hazra and Huser (2021), we fit a linear regression on the raw data using a design matrix including an intercept, linear time trend and bases of 12 cyclic cubic splines (one per month). Taking the fitted values as the mean structure, we estimate the sitewise standard deviations via optimizing the negative log-likelihood of the residuals from the linear fit. Then, seasonality is removed by centering the sitewise data by the estimated mean and standardizing by the standard deviations; see Appendix B.1 for more details.

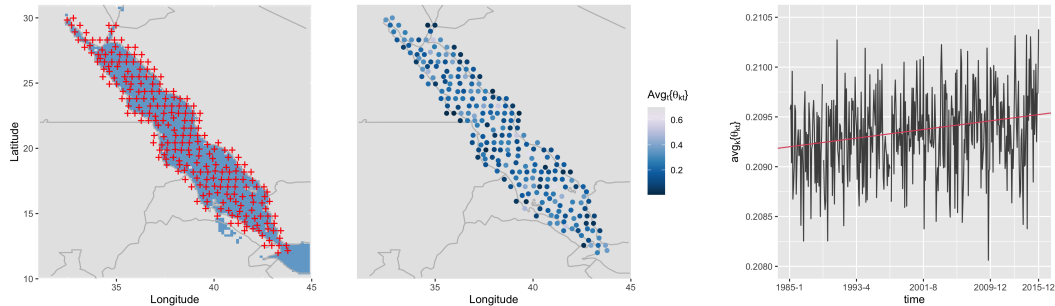


Figure 10: The data-driven knots for the extVAE emulations of the Red Sea SST.

Although the simulation results in Section 5 demonstrate that our extVAE performs well even when the data input is not generated from the process (2), we still extract the monthly maxima from the normalized data to the max-infinite divisibility and enables more accurate modeling of the marginal distributions of station records. In Appendix B.2, we perform various goodness-of-fit tests of the generalized extreme value (GEV) distribution and the general non-central  $t$  distribution, and find that the former fits the monthly maxima very well at almost all grid points (99.99% of 16,703 locations), whereas the general non-central  $t$  distribution, which was used to model the marginal distributions of the daily data in Hazra and Huser (2021), failed to yield MLE parameter estimates at many locations. Therefore, we fit a GEV distribution at each location and transform the sitewise records to the uniform scale to obtain the copula on which we will apply the extVAE.

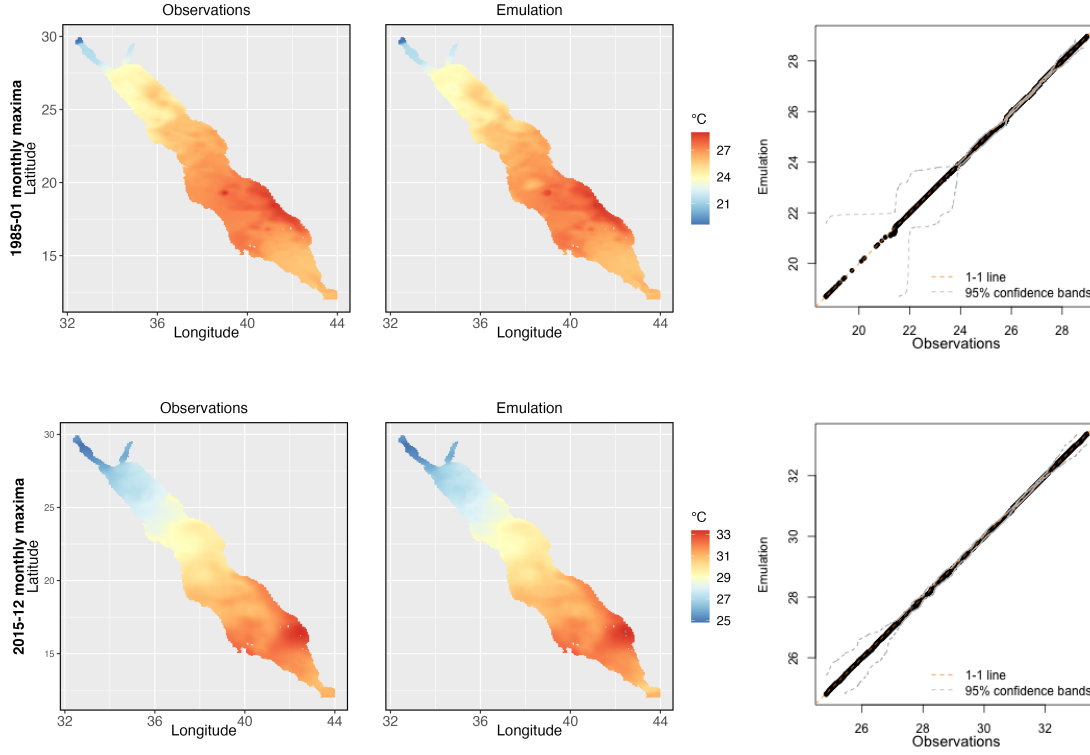


Figure 11: Using the extVAE to emulate the Red Sea SST monthly maxima, we show the results for the months of 1985-01 and 2015-12. From the middle panels (emulation maps) and right panels (QQ plots), we see that the emulated spatial fields match with the observations very well.

The left panel of Figure 10 displays the locations of the data-driven knots chosen by our algorithm, and the initial radius shared by the Wendland basis functions is 1.2 (see Section 5.1 for details on how to select the initial radius). Figure 11 shows that the two emulated replicates for the original monthly maxima field of 1985-01 and 2015-12, which are the beginning and end of the time span of our data set. Here, we convert the emulated copula values to the original data scale using the GEV parameters fitted from the previous step. Figure 11 demonstrates that the extVAE was able to capture the detailed features of the temperature fields and characterize the spatial dependence, and the QQ-plot line show almost perfect alignment with the 1-1 line.

Similar to Figure 7, we estimate the  $\chi_h(u)$  empirically for the original monthly maxima fields and the emulated fields, assuming stationarity and isotropy. Figure 12 attests once more that our extVAE can characterize the extremal dependence structure very accurately both at the low and high quantiles.

As introduced in Section 4.2, we now examine the pairwise  $\chi$  measure to avoid the stationarity assumption. More specifically, we choose the center of the Red Sea (38.104°E, 21.427°N) as a reference point denoted by  $\mathbf{s}_0$ . For all  $\mathbf{s} \in \mathcal{S}$ , we estimate the pairwise  $\chi_{\mathbf{s}_0, \mathbf{s}}(u)$  empirically only using the values from these two locations. Figure 13 is a raster



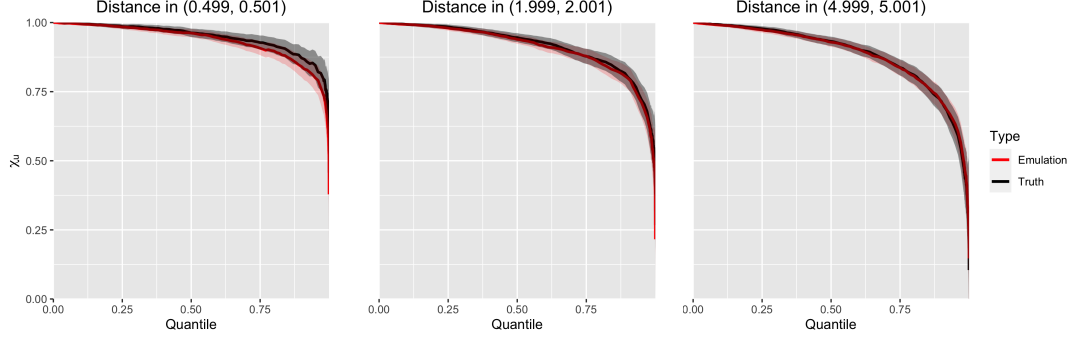


Figure 12: The empirically-estimated tail dependence measure  $\chi_h(u)$  for  $h = 0.5, 2, 5$  ( $\approx 50\text{km}, 200\text{km}, 500\text{km}$ ) for the Red Sea SST monthly maxima and the emulations.

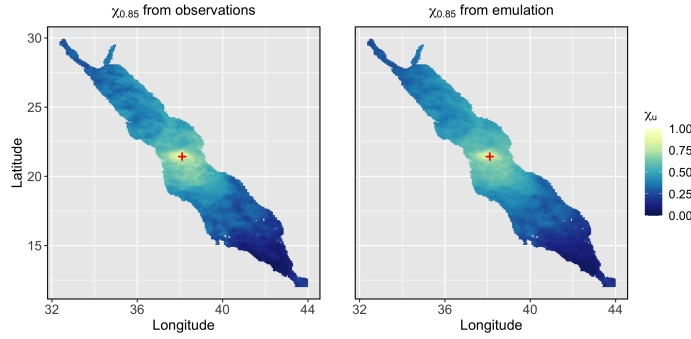


Figure 13: The empirically-estimated pairwise tail dependence measure  $\chi_{s_0,s}(u)$ ,  $u = 0.85$ , where  $s_0 = (38.104, 21.427)$

plot of the pairwise measure evaluated at  $u = 0.85$ . We see that the  $\chi_{s_0,s}(u)$  values estimated from observed and emulated data are very similar.

One other major advantage of our extVAE framework is that we allow the dependence parameters  $\{\theta_k : k = 1, \dots, K\}$  to change over time and hence extremal dependence structure to be non-stationary over time, which is not possible using **hetGP**. The right two panels of Figure 10 shows the estimated  $\{\theta_{tk} : k = 1, \dots, K, t = 1, \dots, n_t\}$  averaged over time (middle panel) or time (right panel). We see that the  $\theta_{kt}$  values are lower near the coast compared to the interior of the Red Sea, and also  $\theta_{kt}$  is increasing slightly over time on average, indicating more localized extreme events.

## 7 Discussion

In this paper, we build a variational autoencoder that is integrated with a novel max-id model that exhibits flexible extremal dependence properties. The encoder and decoder construct and the trained distributions of the latent variables allows for uncertainty quantification within a Bayesian framework. Meanwhile, we model the tail dependence flexibly as opposed to other ML/Extremes paper (e.g. [Sainsbury-Dale et al., 2022a](#); [Richards and](#)

Huser, 2022). Also, our extVAE is (partially) *interpretable* because we showed the decoder can estimate the dependence parameters accurately.

One aspect of our extVAE that needs improving is that the latent PS variables are independent over space and time, which is an unrealistic assumption for physical processes that exhibit diffusive dynamics at short-time scales. For future work, we can include a time component with data-driven dynamic learning focused on a stochastic dynamic spatio-temporal model in a basis representation. Thereby the latent variables in the encoded space evolve over time while retaining their heavy Pareto-like tails and thus ensuring local extremal dependence. The prospect of an integrated spatio-temporal dynamic extreme CVAE is exciting, and if successful, it may be widely applicable in studying daily extreme weather events and providing a novel statistical approach to weather prediction.

Another promising direction of future work is to implement a conditional VAE (Sohn et al., 2015, CVAE) with the max-id model — we allow changes to the parameters for both the encoder and decoder (denoted by  $\Theta$ ) conditioning on different climate scenarios (radiative forcings, seasons, soil conditions, etc.) Firstly, we will simulate the data set under different conditions with more locations and time replicates and re-run the entire CVAE. Then we need to ensure that the conditional VAE will emulate  $\mathbf{X}_t$  differently according to different input states denoted by  $\mathbf{c}_t$  (e.g., tuning parameters and/or forcing variables). Importantly, we allow changes to the parameters for both the encoder and decoder conditioning on different scenarios (e.g., different climate states). This can be achieved by conditioning the encoder and the decoder on  $\mathbf{c}_t$ ; that is, the encoder and the decoder is now each conditioned to two variables:  $q_{\phi_e}(\mathbf{z}_t|\mathbf{x}_t, \mathbf{c}_t)$  and  $p_{\phi_d}(\mathbf{x}_t|\mathbf{z}_t, \mathbf{c}_t)$ . In this way, we can re-formulate the ELBO function such that we can obtain optimum parameters  $\Theta$  that are also conditioned on  $\mathbf{c}_t$ . Eventually, we can efficiently generate data  $\mathbf{X}_t^*$  under an un-observed new input  $\mathbf{c}_t^*$ .

## References

- Allouche, M., Girard, S., and Gobet, E. (2021), “On the approximation of extreme quantiles with ReLU neural networks,” in *EVA 2021-12th International Conference on Extreme Value Analysis*.
- (2022), “EV-GAN: Simulation of extreme events with ReLU neural networks,” *Journal of Machine Learning Research*, 23, 1–39.
- Binois, M. and Gramacy, R. B. (2021), “hetGP: Heteroskedastic Gaussian Process Modeling and Sequential Design in R,” *Journal of Statistical Software*, 98, 1–44.
- Bopp, G. P., Shaby, B. A., and Huser, R. (2021), “A hierarchical max-infinitely divisible spatial model for extreme precipitation,” *Journal of the American Statistical Association*, 116, 93–106.
- Boulaguiem, Y., Zscheischler, J., Vignotto, E., van der Wiel, K., and Engelke, S. (2022), “Modeling and simulating spatial extremes by combining extreme value theory with generative adversarial networks,” *Environmental Data Science*, 1, e5.

- Cartwright, L., Zammit-Mangion, A., and Deutscher, N. M. (2023), “Emulation of greenhouse-gas sensitivities using variational autoencoders,” *Environmetrics*, 34, e2754.
- Castro-Camilo, D. and Huser, R. (2020), “Local likelihood estimation of complex tail dependence structures, applied to US precipitation extremes,” *Journal of the American Statistical Association*, 115, 1037–1054.
- de Haan, L. and Ferreira, A. (2006), *Extreme value theory: an introduction*, vol. 3, Springer.
- Devroye, L. (2009), “Random variate generation for exponentially and polynomially tilted stable distributions,” *ACM Transactions on Modeling and Computer Simulation (TOMACS)*, 19, 1–20.
- Falbel, D. and Luraschi, J. (2023), *torch: Tensors and Neural Networks with ‘GPU’ Acceleration*, <https://torch.mlverse.org/docs>, <https://github.com/mlverse/torch>.
- Ferreira, A. and de Haan, L. (2014), “The generalized Pareto process; with a view towards application and simulation,” *Bernoulli*, 20, 1717 – 1737.
- Francom, D., Sansó, B., Bulaevskaya, V., Lucas, D., and Simpson, M. (2019), “Inferring atmospheric release characteristics in a large computer experiment using Bayesian adaptive splines,” *Journal of the American Statistical Association*.
- Golaz, J.-C., Caldwell, P. M., Van Roekel, L. P., Petersen, M. R., Tang, Q., Wolfe, J. D., Abeshu, G., Anantharaj, V., Asay-Davis, X. S., Bader, D. C., et al. (2019), “The DOE E3SM coupled model version 1: Overview and evaluation at standard resolution,” *Journal of Advances in Modeling Earth Systems*, 11, 2089–2129.
- Gramacy, R. B. (2020), *Surrogates: Gaussian process modeling, design, and optimization for the applied sciences*, Chapman and Hall/CRC.
- Gu, M., Wang, X., and Berger, J. O. (2018), “Robust Gaussian stochastic process emulation,” *The Annals of Statistics*, 46, 3038–3066.
- Haarsma, R. J., Roberts, M. J., Vidale, P. L., Senior, C. A., Bellucci, A., Bao, Q., Chang, P., Corti, S., Fučkar, N. S., Guemas, V., et al. (2016), “High resolution model intercomparison project (HighResMIP v1. 0) for CMIP6,” *Geoscientific Model Development*, 9, 4185–4208.
- Hazra, A. and Huser, R. (2021), “Estimating high-resolution Red Sea surface temperature hotspots, using a low-rank semiparametric spatial model,” *The Annals of Applied Statistics*, 15, 572–596.
- Hougaard, P. (1986), “Survival models for heterogeneous populations derived from stable distributions,” *Biometrika*, 73, 387–396.
- Huser, R. and Wadsworth, J. L. (2019), “Modeling spatial processes with unknown extremal dependence class,” *Journal of the American Statistical Association*, 114, 434–444.

- (2020), “Advances in statistical modeling of spatial extremes,” *Wiley Interdisciplinary Reviews: Computational Statistics*, e1537.
- (2022), “Advances in statistical modeling of spatial extremes,” *Wiley Interdisciplinary Reviews: Computational Statistics*, 14, e1537.
- Kasim, M., Watson-Parris, D., Deaconu, L., Oliver, S., Hatfield, P., Froula, D., Gregori, G., Jarvis, M., Khatiwala, S., Korenaga, J., et al. (2020), “Up to two billion times acceleration of scientific simulations with deep neural architecture search,” in *APS division of plasma physics meeting abstracts*, vol. 2020, pp. BO05–001.
- Kennedy, M. C. and O’Hagan, A. (2001), “Bayesian calibration of computer models,” *Journal of the Royal Statistical Society: Series B (Statistical Methodology)*, 63, 425–464.
- Keydana, S. (2023), *Deep Learning and Scientific Computing with R torch*, CRC Press.
- Kingma, D. P. and Ba, J. (2014), “Adam: A method for stochastic optimization,” *arXiv preprint arXiv:1412.6980*.
- Kingma, D. P. and Welling, M. (2013), “Auto-encoding variational bayes,” *arXiv preprint arXiv:1312.6114*.
- Kingma, D. P., Welling, M., et al. (2019), “An introduction to variational autoencoders,” *Foundations and Trends® in Machine Learning*, 12, 307–392.
- Lafon, N., Naveau, P., and Fablet, R. (2023), “A VAE approach to sample multivariate extremes,” *Hal science preprint*.
- Ledford, A. W. and Tawn, J. A. (1996), “Statistics for near independence in multivariate extreme values,” *Biometrika*, 83, 169–187.
- Malagon-Borja, L. and Fuentes, O. (2009), “Object detection using image reconstruction with PCA,” *Image and Vision Computing*, 27, 2–9.
- Matheson, J. E. and Winkler, R. L. (1976), “Scoring rules for continuous probability distributions,” *Management science*, 22, 1087–1096.
- McDonald, A., Tan, P.-N., and Luo, L. (2022), “Comet flows: Towards generative modeling of multivariate extremes and tail dependence,” *arXiv preprint arXiv:2205.01224*.
- Nolan, J. P. (2020), “Univariate stable distributions,” *Springer Series in Operations Research and Financial Engineering*, DOI, 10, 978–3.
- Pillow, J. W. and Simoncelli, E. P. (2006), “Dimensionality reduction in neural models: an information-theoretic generalization of spike-triggered average and covariance analysis,” *Journal of vision*, 6, 9–9.
- Polyak, B. T. (1964), “Some methods of speeding up the convergence of iteration methods,” *Ussr computational mathematics and mathematical physics*, 4, 1–17.

- Reich, B. J. and Shaby, B. A. (2012), “A hierarchical max-stable spatial model for extreme precipitation,” *The annals of applied statistics*, 6, 1430–1451.
- Richards, J. and Huser, R. (2022), “A unifying partially-interpretable framework for neural network-based extreme quantile regression,” *arXiv preprint arXiv:2208.07581*.
- Richards, J., Sainsbury-Dale, M., Zammit-Mangion, A., and Huser, R. (2023), “Likelihood-free neural Bayes estimators for censored peaks-over-threshold models,” *arXiv preprint arXiv:2306.15642*.
- Sainsbury-Dale, M., Zammit-Mangion, A., and Huser, R. (2022a), “Fast Optimal Estimation with Intractable Models using Permutation-Invariant Neural Networks,” *arXiv preprint arXiv:2208.12942*.
- (2022b), “Neural Point Estimation for Fast Optimal Likelihood-Free Inference,” *arXiv preprint arXiv:2208.12942*.
- Sargsyan, K. (2017), “Surrogate models for uncertainty propagation and sensitivity analysis,” in *Handbook of uncertainty quantification*, Springer, pp. 673–698.
- Simpson, E. S., Opitz, T., and Wadsworth, J. L. (2020), “High-dimensional modeling of spatial and spatio-temporal conditional extremes using INLA and the SPDE approach,” *arXiv preprint arXiv:2011.04486*.
- Simpson, E. S. and Wadsworth, J. L. (2021), “Conditional modelling of spatio-temporal extremes for Red Sea surface temperatures,” *Spatial Statistics*, 41, 100482.
- Sohn, K., Lee, H., and Yan, X. (2015), “Learning structured output representation using deep conditional generative models,” *Advances in neural information processing systems*, 28.
- Thibaud, E. and Opitz, T. (2015), “Efficient inference and simulation for elliptical Pareto processes,” *Biometrika*, 102, 855–870.
- Tieleman, T., Hinton, G., et al. (2012), “Lecture 6.5-rmsprop: Divide the gradient by a running average of its recent magnitude,” *COURSERA: Neural networks for machine learning*, 4, 26–31.
- Wadsworth, J. L. and Tawn, J. (2022), “Higher-dimensional spatial extremes via single-site conditioning,” *Spatial Statistics*, 51, 100677.
- Wendland, H. (1995), “Piecewise polynomial, positive definite and compactly supported radial functions of minimal degree,” *Advances in computational Mathematics*, 4, 389–396.
- Zhang, L., Risser, M. D., Molter, E. M., Wehner, M. F., and O’Brien, T. A. (2022a), “Accounting for the spatial structure of weather systems in detected changes in precipitation extremes,” *Weather and Climate Extremes*, 38, 100499.

Zhang, L., Shaby, B. A., and Wadsworth, J. L. (2022b), “Hierarchical Transformed Scale Mixtures for Flexible Modeling of Spatial Extremes on Datasets with Many Locations,” *J. Amer. Statist. Assoc.*, 117, 1357–1369.

# Appendix

## A Technical details

### A.1 Properties of exponentially tilted positive-stable variables

Before we proceed to prove Proposition 2.1, we first recall some useful results in Hougaard (1986) about positive-stable (PS) distributions and their exponentially tilted variation. If  $Z \sim H(\alpha, \alpha, 0)$ , we denote the density function by  $f_\alpha(z)$ ,  $z > 0$ . Then for  $\alpha \in (0, 1]$ , it has Laplace transform

$$L(s) = Ee^{-sZ} = e^{-s^\alpha}, \quad s \geq 0.$$

If  $Z \sim H(\alpha, \delta, 0)$ , the Laplace transform becomes  $L(s) = \exp(-\delta s^\alpha/\alpha)$ ,  $\delta > 0$ . Further, the exponentially tilted  $Z \sim H(\alpha, \delta, \theta)$  has the Laplace transform

$$L(s) = Ee^{-sZ} = \exp \left[ -\frac{\delta}{\alpha} \{(\theta + s)^\alpha - \theta^\alpha\} \right], \quad s \geq 0, \quad \theta \geq 0 \quad (16)$$

and its density is

$$\frac{f_\alpha \{x/(\delta/\alpha)^{1/\alpha}\} \exp(-\theta x)}{(\delta/\alpha)^{1/\alpha} \exp(-\delta\theta^\alpha/\alpha)}, \quad x > 0.$$

**Lemma A.1.** *If  $Z \sim H(\alpha, \delta, 0)$  and  $\alpha \in (0, 1)$ , then  $Z \sim \text{Stable} \left\{ \alpha, 1, \left( \frac{\delta}{\alpha} \cos \frac{\pi\alpha}{2} \right)^{\frac{1}{\alpha}}, 0; 1 \right\}$ .*

*Proof.* From Proposition 3.2 of Nolan (2020), we know that the Laplace transform of  $Z \sim \text{Stable}(\alpha, 1, \gamma, 0; 1)$ ,  $\alpha \in (0, 2]$ , is

$$Ee^{-sZ} = \begin{cases} \exp\{-\gamma^\alpha (\sec \frac{\pi\alpha}{2}) s^\alpha\}, & \alpha \in (0, 1) \cup (1, 2], \\ \exp\{-\gamma \frac{2}{\pi} s \log s\}, & \alpha = 1. \end{cases}$$

If  $\gamma = |\frac{\delta}{\alpha} \cos \frac{\pi\alpha}{2}|^{1/\alpha}$ , the Laplace transform becomes

$$Ee^{-sZ} = \begin{cases} \exp(-\frac{\delta}{\alpha} s^\alpha), & \alpha \in (0, 1), \\ \exp(\frac{\delta}{\alpha} s^\alpha), & \alpha \in (1, 2]. \end{cases}$$

Therefore we have  $Z \sim \text{Stable}\{\alpha, 1, (\frac{\delta}{\alpha} \cos \frac{\pi\alpha}{2})^{\frac{1}{\alpha}}, 0; 1\}$  when  $\alpha \in (0, 1)$  and  $Z \sim H(\alpha, \delta, 0)$ . □

**Remark 1.** *If  $\alpha = 1/2$ ,  $|\cos \frac{\pi\alpha}{2}|^{1/\alpha} = 1/2$  and  $Z \sim \text{Stable}(1/2, 1, 1/2, 0; 1)$ , which is equivalent to  $Z \sim \text{Lévy}(0, 1/2)$  or  $Z \sim \text{InvGamma}(1/2, 1/4)$ .*



## A.2 Proof of Proposition 2.1

*Proof of Proposition 2.1.* Since at the location  $\mathbf{s}_j$ ,

$$\begin{aligned} \Pr(X_t(\mathbf{s}_j) \leq x) &= E \left\{ \Pr \left( \epsilon_t(\mathbf{s}_j) \leq \frac{x}{Y_t(\mathbf{s}_j)} \middle| Z_{1t}, \dots, Z_{Kt} \right) \right\} \\ &= E \left[ \exp \left\{ - \left( \frac{\tau Y_t(\mathbf{s}_j)}{x} \right)^{\frac{1}{\alpha_0}} \right\} \middle| Z_{1t}, \dots, Z_{Kt} \right] \\ &= E \exp \left\{ - \left( \frac{\tau}{x} \right)^{\frac{1}{\alpha_0}} \sum_{k=1}^K \omega_k(\mathbf{s}_j, r_k)^{\frac{1}{\alpha}} Z_{kt} \right\} \\ &= \exp \left[ \sum_{k \in \bar{\mathcal{D}}} \theta_k^\alpha - \sum_{k=1}^K \left\{ \theta_k + \left( \frac{\tau}{x} \right)^{\frac{1}{\alpha_0}} \omega_{kj}^{\frac{1}{\alpha}} \right\}^\alpha \right]. \end{aligned}$$

To study the tail decay of the survival function, we apply Taylor's expansion with the Peano remainder:

$$(1+t)^\alpha = 1 + \alpha t + \frac{\alpha(\alpha-1)}{2} t^2 + o(t^2), \text{ as } t \rightarrow 0. \quad (17)$$

Then, as  $x \rightarrow \infty$ , we have

$$\begin{aligned} \sum_{k \in \bar{\mathcal{D}}} \left\{ \theta_k + \left( \frac{\tau}{x} \right)^{\frac{1}{\alpha_0}} \omega_{kj}^{\frac{1}{\alpha}} \right\}^\alpha &= \sum_{k \in \bar{\mathcal{D}}} \theta_k^\alpha \left\{ 1 + \left( \frac{\tau}{x} \right)^{\frac{1}{\alpha_0}} \frac{\omega_{kj}^{1/\alpha}}{\theta_k} \right\}^\alpha \\ &= \sum_{k \in \bar{\mathcal{D}}} \theta_k^\alpha + \alpha \left( \frac{\tau}{x} \right)^{\frac{1}{\alpha_0}} \sum_{k \in \bar{\mathcal{D}}} \frac{\omega_{kj}^{1/\alpha}}{\theta_k^{1-\alpha}} + \frac{\alpha(\alpha-1)}{2} \left( \frac{\tau}{x} \right)^{\frac{2}{\alpha_0}} \sum_{k \in \bar{\mathcal{D}}} \frac{\omega_{kj}^{2/\alpha}}{\theta_k^{2-\alpha}} + o \left( x^{-\frac{2}{\alpha_0}} \right), \end{aligned}$$

which leads to

$$\begin{aligned} \sum_{k \in \bar{\mathcal{D}}} \theta_k^\alpha - \sum_{k=1}^K \left\{ \theta_k + \left( \frac{\tau}{x} \right)^{\frac{1}{\alpha_0}} \omega_{kj}^{\frac{1}{\alpha}} \right\}^\alpha &= - \left( \frac{\tau}{x} \right)^{\frac{\alpha}{\alpha_0}} \sum_{k \in \bar{\mathcal{D}}} \omega_{kj} - \alpha \left( \frac{\tau}{x} \right)^{\frac{1}{\alpha_0}} \sum_{k \in \bar{\mathcal{D}}} \frac{\omega_{kj}^{1/\alpha}}{\theta_k^{1-\alpha}} \\ &\quad - \frac{\alpha(\alpha-1)}{2} \left( \frac{\tau}{x} \right)^{\frac{2}{\alpha_0}} \sum_{k \in \bar{\mathcal{D}}} \frac{\omega_{kj}^{2/\alpha}}{\theta_k^{2-\alpha}} + o \left( x^{-\frac{2}{\alpha_0}} \right) = -c'_j x^{-\frac{\alpha}{\alpha_0}} - c_j x^{-\frac{1}{\alpha_0}} - d_j x^{-\frac{2}{\alpha_0}} + o \left( x^{-\frac{2}{\alpha_0}} \right), \end{aligned} \quad (18)$$

where the constants  $c'_j$ ,  $c_j$  and  $d_j$  are defined in (7).

Next we apply the following Taylor expansion:

$$1 - \exp(-t) = t - \frac{t^2}{2} + o(t^2), \text{ as } t \rightarrow 0.$$

Combining (5) and (18) gives

$$\bar{F}_j(x) = c'_j x^{-\frac{\alpha}{\alpha_0}} + c_j x^{-\frac{1}{\alpha_0}} + d_j x^{-\frac{2}{\alpha_0}} - \frac{(c'_j x^{-\frac{\alpha}{\alpha_0}} + c_j x^{-\frac{1}{\alpha_0}} + d_j x^{-\frac{2}{\alpha_0}})^2}{2} + o \left( x^{-\frac{2}{\alpha_0}} \right),$$

from which we can expand the squared term and discard the terms with higher decaying rates than  $o(x^{-2/\alpha_0})$  to establish (6). □

*Proof of Corollary 2.1.2.* By definition,  $t^{-1} = \bar{F}_j\{q_j(t)\}$ . When  $\mathcal{C}_j \cap \mathcal{D} \neq \emptyset$ , (6) leads to

$$t^{-1} = c'_j q_j^{-\frac{\alpha}{\alpha_0}}(t) \left[ 1 + \frac{c_j}{c'_j} q_j^{-\frac{1-\alpha}{\alpha_0}}(t) + \frac{1}{c'_j} \left( d_j - \frac{c_j^2}{2} \right) q_j^{-\frac{2-\alpha}{\alpha_0}}(t) - \frac{c'_j}{2} q_j^{-\frac{\alpha}{\alpha_0}}(t) - c_j q_j^{-\frac{1}{\alpha_0}}(t) + o \left\{ q_j^{-\frac{1}{\alpha_0}}(t) \right\} \right] \text{ as } t \rightarrow \infty,$$

and thus

$$c'_j \frac{\alpha_0}{\alpha} t^{\frac{\alpha_0}{\alpha}} = q_j(t) \left[ 1 + \frac{c_j}{c'_j} q_j^{-\frac{1-\alpha}{\alpha_0}}(t) + \frac{1}{c'_j} \left( d_j - \frac{c_j^2}{2} \right) q_j^{-\frac{2-\alpha}{\alpha_0}}(t) - \frac{c'_j}{2} q_j^{-\frac{\alpha}{\alpha_0}}(t) - c_j q_j^{-\frac{1}{\alpha_0}}(t) + o \left\{ q_j^{-\frac{1}{\alpha_0}}(t) \right\} \right]^{-\frac{\alpha_0}{\alpha}} \text{ as } t \rightarrow \infty. \quad (19)$$

Since  $q_j(t) \rightarrow \infty$  as  $t \rightarrow \infty$ , we can apply the Taylor expansion in (17) again to show that the term in squared brackets with an exponent of  $-\alpha_0/\alpha$  on the right-hand side of the previous display can simply be approximated by  $1 + o(1)$ . Thus, we have

$$q_j(t) = c'_j \frac{\alpha_0}{\alpha} t^{\frac{\alpha_0}{\alpha}} \{1 + o(1)\}.$$

Plugging this back into (19), we obtain

$$\begin{aligned} q_j(t) - c'_j \frac{\alpha_0}{\alpha} t^{\frac{\alpha_0}{\alpha}} &= q_j(t) \left( 1 - \left[ 1 + \frac{c_j}{c'_j} q_j^{-\frac{1-\alpha}{\alpha_0}}(t) + o \left\{ q_j^{-\frac{1-\alpha}{\alpha_0}}(t) \right\} \right]^{-\frac{\alpha_0}{\alpha}} \right) \\ &= q_j(t) \left[ \frac{\alpha_0 c_j}{\alpha c'_j} q_j^{-\frac{1-\alpha}{\alpha_0}}(t) + o \left\{ q_j^{-\frac{1-\alpha}{\alpha_0}}(t) \right\} \right] \\ &= c'_j \frac{\alpha_0}{\alpha} t^{\frac{\alpha_0}{\alpha}} \{1 + o(1)\} \left\{ \frac{\alpha_0 c_j}{\alpha c'_j 1/\alpha} t^{1-\frac{1}{\alpha}} + o \left( t^{1-\frac{1}{\alpha}} \right) \right\} \\ &= c'_j \frac{\alpha_0}{\alpha} t^{\frac{\alpha_0}{\alpha}} \left\{ \frac{\alpha_0 c_j}{\alpha c'_j 1/\alpha} t^{1-\frac{1}{\alpha}} + o \left( t^{1-\frac{1}{\alpha}} \right) \right\} \end{aligned}$$

Similarly, when  $\mathcal{C}_j \cap \mathcal{D} = \emptyset$ , we have

$$c_j^{\alpha_0} t^{\alpha_0} = q_j(t) \left[ 1 + \left( \frac{d_j}{c_j} - \frac{c_j}{2} \right) q_j^{-\frac{1}{\alpha_0}}(t) + o \left\{ q_j^{-\frac{1}{\alpha_0}}(t) \right\} \right]^{-\alpha_0} \text{ as } t \rightarrow \infty,$$

which ensures

$$q_j(t) = c_j^{\alpha_0} t^{\alpha_0} \{1 + o(1)\},$$

and

$$\begin{aligned} q_j(t) - c_j^{\alpha_0} t^{\alpha_0} &= q_j(t) \left( 1 - \left[ 1 + \left( \frac{d_j}{c_j} - \frac{c_j}{2} \right) q_j^{-\frac{1}{\alpha_0}}(t) + o \left\{ q_j^{-\frac{1}{\alpha_0}}(t) \right\} \right]^{-\alpha_0} \right) \\ &= c_j^{\alpha_0} t^{\alpha_0} \{1 + o(1)\} \left[ \alpha_0 \left( \frac{d_j}{c_j} - \frac{c_j}{2} \right) q_j^{-\frac{1}{\alpha_0}}(t) + o \left\{ q_j^{-\frac{1}{\alpha_0}}(t) \right\} \right] \\ &= c_j^{\alpha_0} t^{\alpha_0} \left\{ \alpha_0 \left( \frac{d_j}{c_j^2} - \frac{1}{2} \right) t^{-1} + o(t^{-1}) \right\} \end{aligned}$$

□

### A.3 Proof of Proposition 2.2

*Proof of Proposition 2.2.* From (16), the joint distribution for the discretization of  $\{X_t(\mathbf{s}), \mathbf{s} \in \mathcal{D}\}$  is

$$\begin{aligned}
F(x_1, \dots, x_n) &= \Pr(X_t(\mathbf{s}_1) \leq x_1, \dots, X_t(\mathbf{s}_n) \leq x_n) \\
&= E \left\{ \Pr \left( \epsilon_t(\mathbf{s}_1) \leq \frac{x_1}{Y_t(\mathbf{s}_1)}, \dots, \epsilon_t(\mathbf{s}_n) \leq \frac{x_n}{Y_t(\mathbf{s}_n)} \middle| Z_{1t}, \dots, Z_{Kt} \right) \right\} \\
&= E \left[ \prod_{j=1}^n \exp \left\{ - \left( \frac{\tau Y_t(\mathbf{s}_j)}{x_j} \right)^{\frac{1}{\alpha_0}} \right\} \middle| Z_{1t}, \dots, Z_{Kt} \right] \\
&= \prod_{k=1}^K E \exp \left\{ - \sum_{j=1}^{n_s} \omega_k(\mathbf{s}_j, r_k)^{\frac{1}{\alpha}} \left( \frac{\tau}{x_j} \right)^{\frac{1}{\alpha_0}} Z_{kt} \right\} \\
&= \exp \left[ \sum_{k \in \bar{\mathcal{D}}} \theta_k^\alpha - \sum_{k=1}^K \left\{ \theta_k + \tau^{\frac{1}{\alpha_0}} \sum_{j=1}^{n_s} \frac{\omega_{kj}^{1/\alpha}}{x_j^{1/\alpha_0}} \right\}^\alpha \right].
\end{aligned}$$

□

### A.4 Proof of Theorem 2.3

*Proof of Theorem 2.3.* By definition of the upper tail dependence measure,

$$\begin{aligned}
\chi(\mathbf{s}_i, \mathbf{s}_j) &= \lim_{u \rightarrow 1} \frac{\Pr\{X(\mathbf{s}_i) > F_i^{-1}(u), X(\mathbf{s}_j) > F_j^{-1}(u)\}}{1 - u} \\
&= \lim_{t \rightarrow \infty} t \Pr\{X(\mathbf{s}_i) > q_i(t), X(\mathbf{s}_j) > q_j(t)\} \\
&= \lim_{t \rightarrow \infty} t \left[ 1 - 2 \left( 1 - \frac{1}{t} \right) + \Pr\{X(\mathbf{s}_i) \leq q_i(t), X(\mathbf{s}_j) \leq q_j(t)\} \right] \\
&= \lim_{t \rightarrow \infty} 2 - t [1 - F_{ij}\{q_i(t), q_j(t)\}]
\end{aligned} \tag{20}$$

and

$$\Pr\{X(\mathbf{s}_i) > q_i(t), X(\mathbf{s}_j) > q_j(t)\} = \mathcal{L}(t) t^{-1/\eta(\mathbf{s}_i, \mathbf{s}_j)}, \quad t \rightarrow \infty. \tag{21}$$

(a) If  $\mathcal{C}_i \cap \mathcal{D} = \emptyset$  and  $\mathcal{C}_j \cap \mathcal{D} = \emptyset$ , we know from Corollary 2.1.2 that  $q_i(t) = c_i^{\alpha_0} t^{\alpha_0} \{1 +$

$O(t^{-1})\}$  and  $q_j(t) = c_j^{\alpha_0} t^{\alpha_0} \{1 + O(t^{-1})\}$ . Similarly to Proposition 2.1, we first deduce

$$\begin{aligned}
\log F_{ij}\{q_i(t), q_j(t)\} &= \sum_{k \in \bar{\mathcal{D}}} \theta_k^\alpha - \sum_{k \in \bar{\mathcal{D}}} \left[ \theta_k + \frac{\tau^{1/\alpha_0} \omega_{ki}^{1/\alpha}}{c_i t \{1 + O(t^{-1})\}} + \frac{\tau^{1/\alpha_0} \omega_{kj}^{1/\alpha}}{c_j t \{1 + O(t^{-1})\}} \right]^\alpha \\
&= \sum_{k \in \bar{\mathcal{D}}} \theta_k^\alpha - \sum_{k \in \bar{\mathcal{D}}} \theta_k^\alpha \left[ 1 + \frac{\tau^{1/\alpha_0} \omega_{ki}^{1/\alpha} / \theta_k}{c_i t} + \frac{\tau^{1/\alpha_0} \omega_{kj}^{1/\alpha} / \theta_k}{c_j t} + O\left(\frac{1}{t^2}\right) \right]^\alpha \\
&= \sum_{k \in \bar{\mathcal{D}}} \theta_k^\alpha - \sum_{k \in \bar{\mathcal{D}}} \theta_k^\alpha \left[ 1 + \frac{\alpha \tau^{1/\alpha_0} \omega_{ki}^{1/\alpha} / \theta_k}{c_i t} + \frac{\alpha \tau^{1/\alpha_0} \omega_{kj}^{1/\alpha} / \theta_k}{c_j t} + O\left(\frac{1}{t^2}\right) \right] \\
&= -\frac{2}{t} - O\left(\frac{1}{t^2}\right) \text{ as } t \rightarrow \infty.
\end{aligned}$$

It follows that

$$1 - F_{ij}\{q_i(t), q_j(t)\} = 1 - \exp\left\{-\frac{2}{t} - O\left(\frac{1}{t^2}\right)\right\} = \frac{2}{t} + O\left(\frac{1}{t^2}\right).$$

Then from (20) we know that  $\chi(\mathbf{s}_i, \mathbf{s}_j) = \lim_{t \rightarrow \infty} O(t^{-1}) = 0$ .

In the meantime,

$$\log \Pr\{X(\mathbf{s}_i) > q_i(t), X(\mathbf{s}_j) > q_j(t)\} = -2 \log(t) \text{ as } t \rightarrow \infty$$

and  $\eta(\mathbf{s}_i, \mathbf{s}_j) = 1/2$ .

- (b) If  $\mathcal{C}_i \cap \mathcal{D} = \emptyset$  and  $\mathcal{C}_j \cap \mathcal{D} \neq \emptyset$ , we know from Corollary 2.1.2 that  $q_i(t) \sim c_i^{\alpha_0} t^{\alpha_0} \{1 + R_i(t)\}$  and  $q_j(t) \sim c_j^{\alpha_0/\alpha} t^{\alpha_0/\alpha} \{1 + R_j(t)\}$  as  $t \rightarrow \infty$ . Then

$$\begin{aligned}
\log F_{ij}\{q_i(t), q_j(t)\} &= \sum_{k \in \bar{\mathcal{D}}} \theta_k^\alpha - \sum_{k=1}^K \left\{ \theta_k + \frac{\tau^{1/\alpha_0} \omega_{ki}^{1/\alpha}}{q_i^{1/\alpha_0}(t)} + \frac{\tau^{1/\alpha_0} \omega_{kj}^{1/\alpha}}{q_j^{1/\alpha_0}(t)} \right\}^\alpha \\
&= \sum_{k \in \bar{\mathcal{D}}} \theta_k^\alpha - \sum_{k \in \bar{\mathcal{D}}} \left\{ \theta_k + \frac{\tau^{1/\alpha_0} \omega_{ki}^{1/\alpha}}{q_i^{1/\alpha_0}(t)} + \frac{\tau^{1/\alpha_0} \omega_{kj}^{1/\alpha}}{q_j^{1/\alpha_0}(t)} \right\}^\alpha - \sum_{k \in \mathcal{D}} \frac{\tau^{\alpha/\alpha_0} \omega_{kj}}{q_j^{\alpha/\alpha_0}(t)} \\
&= \sum_{k \in \bar{\mathcal{D}}} \theta_k^\alpha - \sum_{k \in \bar{\mathcal{D}}} \left[ \theta_k^\alpha + \frac{\alpha \tau^{1/\alpha_0} \omega_{ki}^{1/\alpha}}{\theta^{1-\alpha} q_i^{1/\alpha_0}(t)} + \frac{\alpha \tau^{1/\alpha_0} \omega_{kj}^{1/\alpha}}{\theta^{1-\alpha} q_j^{1/\alpha_0}(t)} + \frac{d_i}{q_i^{2/\alpha_0}(t)} + O(t^{-1-1/\alpha}) \right] - \sum_{k \in \mathcal{D}} \frac{\tau^{\alpha/\alpha_0} \omega_{kj}}{q_j^{\alpha/\alpha_0}(t)} \\
&= -\frac{c_i}{q_i^{1/\alpha_0}(t)} - \frac{c_j}{q_j^{1/\alpha_0}(t)} - \frac{c_j'}{q_j^{\alpha/\alpha_0}(t)} - \frac{d_i}{q_i^{2/\alpha_0}(t)} - O(t^{-1-1/\alpha}), \text{ as } t \rightarrow \infty.
\end{aligned}$$

It follows from (20) that

$$\begin{aligned}
1 - F_{ij}\{q_i(t), q_j(t)\} &= 1 - \exp \left[ -\frac{c_i}{q_i^{1/\alpha_0}(t)} - \frac{c_j}{q_j^{1/\alpha_0}(t)} - \frac{c'_j}{q_j^{\alpha/\alpha_0}(t)} - \frac{d_i}{q_i^{2/\alpha_0}(t)} - O(t^{-1-1/\alpha}) \right] \\
&= \frac{c_i}{q_i^{1/\alpha_0}(t)} + \frac{c_j}{q_j^{1/\alpha_0}(t)} + \frac{c'_j}{q_j^{\alpha/\alpha_0}(t)} + \left( d_i - \frac{c_i^2}{2} \right) \frac{1}{q_i^{2/\alpha_0}(t)} + O(t^{-1-1/\alpha}) \\
&= \frac{1}{t\{1 + R_i(t)\}^{1/\alpha_0}} + \frac{c_j}{c_j^{1/\alpha} t^{1/\alpha} \{1 + R_j(t)\}^{1/\alpha_0}} + \frac{1}{t\{1 + R_j(t)\}^{\alpha/\alpha_0}} + \\
&\quad \left( \frac{d_i}{c_i^2} - \frac{1}{2} \right) \frac{1}{t^2 \{1 + R_i(t)\}^{2/\alpha_0}} + O(t^{-1-1/\alpha}) \\
&= \frac{1}{t\{1 + \alpha_0^{-1} R_i(t)\}} + \frac{c_j}{c_j^{1/\alpha} t^{1/\alpha} \{1 + \alpha_0^{-1} R_j(t)\}} + \frac{1}{t\{1 + \frac{\alpha}{\alpha_0} R_j(t)\}} + \\
&\quad \left( \frac{d_i}{c_i^2} - \frac{1}{2} \right) \frac{1}{t^2 \{1 + 2\alpha_0^{-1} R_i(t)\}} + O(t^{-1-1/\alpha})
\end{aligned}$$

and

$$\begin{aligned}
\Pr\{X(\mathbf{s}_i) > q_i(t), X(\mathbf{s}_j) > q_j(t)\} &= \frac{\alpha_0^{-1} R_i(t)}{t\{1 + \alpha_0^{-1} R_i(t)\}} + \frac{\frac{\alpha}{\alpha_0} R_j(t)}{t\{1 + \frac{\alpha}{\alpha_0} R_j(t)\}} - \frac{c_j}{c_j^{1/\alpha} t^{1/\alpha} \{1 + \alpha_0^{-1} R_j(t)\}} - \\
&\quad \left( \frac{d_i}{c_i^2} - \frac{1}{2} \right) \frac{1}{t^2 \{1 + 2\alpha_0^{-1} R_i(t)\}} + O(t^{-1-1/\alpha}) \\
&= O(t^{-1-1/\alpha})
\end{aligned}$$

as  $t \rightarrow \infty$ . Therefore,  $\chi(\mathbf{s}_i, \mathbf{s}_j) = 0$  and  $\eta(\mathbf{s}_i, \mathbf{s}_j) = \alpha/(\alpha + 1)$ .

- (c) When  $\mathcal{C}_i \cap \mathcal{D} \neq \emptyset$  and  $\mathcal{C}_j \cap \mathcal{D} = \emptyset$ , the proof is analogous to the case (b).  
(d) When  $\mathcal{C}_i \cap \mathcal{D} \neq \emptyset$  and  $\mathcal{C}_j \cap \mathcal{D} \neq \emptyset$ , we have  $q_i(t) \sim c_i'^{\alpha_0/\alpha} t^{\alpha_0/\alpha} \{1 + O(t^{1-1/\alpha})\}$  and  $q_j(t) \sim c_j'^{\alpha_0/\alpha} t^{\alpha_0/\alpha} \{1 + O(t^{1-1/\alpha})\}$  as  $t \rightarrow \infty$ . Then

$$\begin{aligned}
\log F_{ij}\{q_i(t), q_j(t)\} &= \sum_{k \in \bar{\mathcal{D}}} \theta_k^\alpha - \sum_{k=1}^K \left\{ \theta_k + \frac{\tau^{1/\alpha_0} \omega_{ki}^{1/\alpha}}{q_i^{1/\alpha_0}(t)} + \frac{\tau^{1/\alpha_0} \omega_{kj}^{1/\alpha}}{q_j^{1/\alpha_0}(t)} \right\}^\alpha \\
&= \sum_{k \in \bar{\mathcal{D}}} \theta_k^\alpha - \sum_{k=1}^K \left[ \theta_k + \frac{\tau^{1/\alpha_0} \omega_{ki}^{1/\alpha} t^{-1/\alpha}}{c_i'^{1/\alpha} \{1 + O(t^{1-1/\alpha})\}^{1/\alpha_0}} + \frac{\tau^{1/\alpha_0} \omega_{kj}^{1/\alpha} t^{-1/\alpha}}{c_j'^{1/\alpha} \{1 + O(t^{1-1/\alpha})\}^{1/\alpha_0}} \right]^\alpha \\
&= \sum_{k \in \bar{\mathcal{D}}} \theta_k^\alpha - \sum_{k=1}^K \left[ \theta_k + \tau^{\frac{1}{\alpha_0}} \left( \frac{\omega_{ki}^{1/\alpha}}{c_i'^{1/\alpha}} + \frac{\omega_{kj}^{1/\alpha}}{c_j'^{1/\alpha}} \right) t^{-\frac{1}{\alpha}} + O\left(t^{1-\frac{2}{\alpha}}\right) \right]^\alpha \\
&= \sum_{k \in \bar{\mathcal{D}}} \theta_k^\alpha - \sum_{k \in \bar{\mathcal{D}}} \left[ \theta_k^\alpha + \frac{\alpha \tau^{1/\alpha_0}}{\theta_k^{1-\alpha}} \left( \frac{\omega_{ki}^{1/\alpha}}{c_i'^{1/\alpha}} + \frac{\omega_{kj}^{1/\alpha}}{c_j'^{1/\alpha}} \right) t^{-\frac{1}{\alpha}} + O\left(t^{1-\frac{2}{\alpha}}\right) \right] - \\
&\quad \tau^{\frac{\alpha}{\alpha_0}} \sum_{k \in \bar{\mathcal{D}}} \left( \frac{\omega_{ki}^{1/\alpha}}{c_i'^{1/\alpha}} + \frac{\omega_{kj}^{1/\alpha}}{c_j'^{1/\alpha}} \right)^\alpha t^{-1} - O(t^{1-\frac{2}{\alpha}}) \\
&= -d_{ij} t^{-1} - \left( \frac{c_i}{c_i'^{1/\alpha}} + \frac{c_j}{c_j'^{1/\alpha}} \right) t^{-\frac{1}{\alpha}} - O(t^{1-\frac{2}{\alpha}}), \text{ as } t \rightarrow \infty.
\end{aligned}$$

It follows from (20) that

$$\begin{aligned} 1 - F_{ij}\{q_i(t), q_j(t)\} &= 1 - \exp \left\{ -d_{ij}t^{-1} - \left( \frac{c_i}{c_i'^{1/\alpha}} + \frac{c_j}{c_j'^{1/\alpha}} \right) t^{-\frac{1}{\alpha}} - O(t^{1-\frac{2}{\alpha}}) \right\} \\ &= d_{ij}t^{-1} + \left( \frac{c_i}{c_i'^{1/\alpha}} + \frac{c_j}{c_j'^{1/\alpha}} \right) t^{-\frac{1}{\alpha}} + O(t^{1-\frac{2}{\alpha}}) \end{aligned}$$

and

$$t \Pr\{X(\mathbf{s}_i) > q_i(t), X(\mathbf{s}_j) > q_j(t)\} = 2 - d_{ij} - \left( \frac{c_i}{c_i'^{1/\alpha}} + \frac{c_j}{c_j'^{1/\alpha}} \right) t^{1-\frac{1}{\alpha}} - O(t^{2-\frac{2}{\alpha}})$$

as  $t \rightarrow \infty$ , in which  $d_{ij}$  is defined in (10).

If  $\mathcal{C}_i \cap \mathcal{C}_j \neq \emptyset$ , we know from (20) that  $\chi(\mathbf{s}_i, \mathbf{s}_j) = 2 - d_{ij} \in (0, 1)$  and

$$\chi_u(\mathbf{s}_i, \mathbf{s}_j) - \chi(\mathbf{s}_i, \mathbf{s}_j) = \left( \frac{c_i}{c_i'^{1/\alpha}} + \frac{c_j}{c_j'^{1/\alpha}} \right) (1 - u)^{\frac{1}{\alpha}-1} + O \left\{ (1 - u)^{\frac{2}{\alpha}-2} \right\}$$

□

## B Red Sea Dataset

### B.1 Remove seasonality

For site  $\mathbf{s}_i$ , we consider the neighborhood  $\mathcal{D}$  of radius  $r$  such that  $\mathcal{D} = \{j : \|\mathbf{s}_i - \mathbf{s}_j\| < r, j = 1, \dots, J\}$ , in practical we set  $r = 30$  km. By an abuse of notation, we let  $\mathbf{y}$  be the response vector with length  $n_t \cdot J$  where  $n_t = 11315$ . Let's construct a matrix  $\mathbf{X}_B = (\mathbf{1}_{n_t}, \mathbf{t}, \mathbf{B}_{n_t \times 12})$  where  $\mathbf{t} = (1, \dots, n_t)/36500$  and  $\mathbf{B}$  is the cubic spline basis of 365 days with knots equal to 12 quantiles of  $(1, \dots, 365)$ , then vertically stack the matrix  $\mathbf{X}_B$   $J$  times to build the design matrix  $\mathbf{X}$ . By fitting the linear regression

$$\mathbf{y} = \mathbf{X}\boldsymbol{\beta}$$

we get the fitted values  $\hat{\mathbf{y}}$ , note that in defining the neighborhood of site  $\mathbf{s}_i$  we also include the  $i$ th site. Then we take the fitted values corresponding to the  $i$ th site as the mean structure.

For modeling the standard deviation, we only use the intercept and time trend which are the first two columns of  $\mathbf{X}$ , we denote it as  $\mathbf{X}_\sigma$ . The estimation of standard deviation is

$$\hat{\sigma}_{\mathbf{s}_i}^2 = \exp(\mathbf{X}_\sigma \times (\hat{\theta}_1, \hat{\theta}_2)')$$

where

$$(\hat{\theta}_1, \hat{\theta}_2) = \underset{(\theta_1, \theta_2)}{\operatorname{argmin}} \sum_{k=1}^{n_t \cdot J} \left[ x_{\sigma, k1} \theta_1 + x_{\sigma, k2} \theta_2 + \frac{1}{2} \cdot \frac{y_k - \hat{y}_k}{\exp(x_{\sigma, k1} \theta_1 + x_{\sigma, k2} \theta_2)} \right]$$

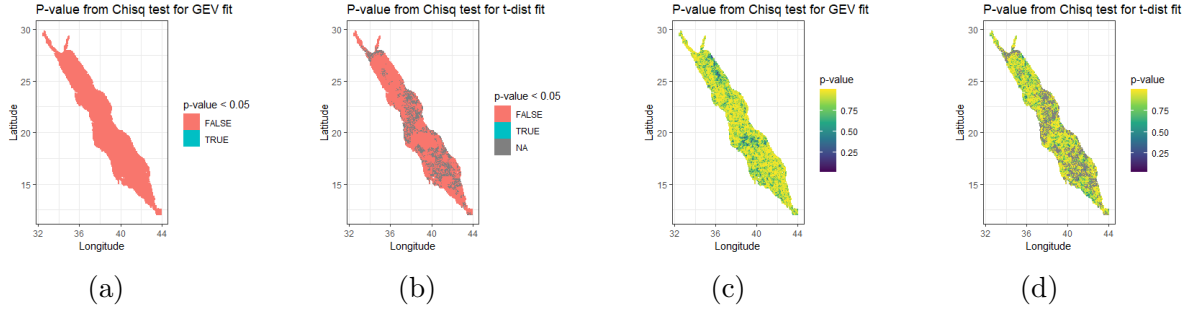


Figure 14: (a): Binary p-values map from  $\chi^2$  GOF test for GEV distribution; (b): Binary p-values map from  $\chi^2$  GOF test for t distribution; (c): Continuous p-values map from  $\chi^2$  GOF test for GEV distribution; (d): Continuous p-values map from  $\chi^2$  GOF test for t distribution.

## B.2 Marginal distributions of the monthly maxima

After we getting rid of seasonality by normalization, we extract monthly maxima according to the setup of our model. We seek for a distribution which fit to the monthly maxima well, then can help us transforming the data to some heavy-tailed distribution, thus our proposed model could be applied. The candidates are Generalized Extreme Value (GEV) distribution and t distribution. We tried different goodness-of-fit (GOF) tests like KS-test, Anderson-Darling test and  $\chi^2$  test, finally  $\chi^2$  test was chosen due to it's flexibility of choosing degrees of freedom as well as the size of intervals. The steps and results are followed:

Calculate the cut points using all the data by set up the number of intervals (set to 20 in practical). For each site, count the observed frequencies  $O_i$  ( $i = 1, \dots, 20$ ) and fit the data to GEV or t distribution to get the parameter estimates. The expected frequencies  $E_i$  ( $i = 1, \dots, 20$ ) is calculated by the CDF increments in each interval multiplying by the number of observations at each site. The  $\chi^2$  statistic is

$$\chi^2_{20-4} = \sum_{i=1}^{20} O_i \log(O_i/E_i)$$

note that we lose 3 degrees of freedom in both GEV (location, scale, shape) and t (location, scale, df) distribution. From the spatial map for p-values shown in Figure 14a, the monthly maxima at all locations pass the  $\chi^2$  test for GEV distribution. For those shaded locations in Figure 14b, there are no parameter estimates for t-distribution. In the Figure 14c, most of locations have p-values greater than 0.75 and outperform what we observed in Figure 14d. This indicates that the GEV distribution would be the better choice to describe the data.

Before applying our model to the dataset, certain transformations need to be done to match our marginals in Section 2.2. In the step of generating the p-value maps, we already estimate the location-wised GEV parameters:  $\mu_i, \sigma_i, \xi_i$ , for  $i = 1, \dots, n_s$ . We observed that the shape parameters  $\xi$  are all negative, so the upper bound of support of GEV distribution could help us with the transformation:



Let

$$\beta_i = \mu_i - \sigma_i/\xi_i$$

and the transformed data  $\{y_{it}^*\}$ ,  $t = 1, \dots, n_t$

$$y_{it}^* = \left( \frac{|\xi_i|(\beta_i - y_{it})}{\sigma_i} \right)^{1/\xi_i}$$

## C Some derivations

Let's use independent Fréchet( $\alpha = 1, s, m$ ) for white noise process  $\epsilon_t(\mathbf{s})$ . Then the c.d.f:

$$P(X_t \leq \mathbf{x}_t | \mathbf{Z}_t) = \exp \left[ - \sum_{i=1}^{n_s} s(x_{it}/y_{it} - m)^{-1} \right]$$

and the p.d.f:

$$P(X_t = \mathbf{x}_t | \mathbf{Z}_t) = s^{n_s} \prod_{i=1}^{n_s} \frac{(x_{it}/y_{it} - m)^{-2}}{y_{it}} \cdot \exp \left[ - \sum_{i=1}^{n_s} s(x_{it}/y_{it} - m)^{-1} \right]$$

then we take logarithm and plug in the low-rank representation of  $Y_t(\mathbf{s})$ :

$$\begin{aligned} \log(P(X_t = \mathbf{x}_t | \mathbf{Z}_t)) &= n_s \log(s) + \sum_{i=1}^{n_s} \left[ -2 \log(x_{it}/y_{it} - m) - \log(y_{it}) - s(x_{it}/y_{it} - m)^{-1} \right] \\ &= n_s \log(s) + \sum_{i=1}^{n_s} \left[ -2 \log \left( \frac{x_{it}}{\sum_{k=1}^K w_{ik}^{1/\alpha} Z_{kt}} - m \right) - \log \left( \sum_{k=1}^K w_{ik}^{1/\alpha} Z_{kt} \right) \right. \\ &\quad \left. - s \left( \frac{x_{it}}{\sum_{k=1}^K w_{ik}^{1/\alpha} Z_{kt}} - m \right)^{-1} \right] \end{aligned}$$

and in finding the appropriate starting values of VAE parameters, we may use the gradient of log-likelihood with respect to the latent variable:

$$\begin{aligned} \frac{\partial \log(P(X_t = \mathbf{x}_t | \mathbf{Z}_t))}{\partial Z_{kt}} &= \sum_{i=1}^{n_s} \left[ -2 \left( \frac{x_{it}}{\sum_{k=1}^K w_{ik}^{1/\alpha} Z_{kt}} - m \right)^{-1} \left( - \frac{x_{it} w_{ik}^{1/\alpha}}{(\sum_{k=1}^K w_{ik}^{1/\alpha} Z_{kt})^2} \right) \right. \\ &\quad \left. - \frac{w_{ik}^{1/\alpha}}{\sum_{k=1}^K w_{ik}^{1/\alpha} Z_{kt}} + s \left( \frac{x_{it}}{\sum_{k=1}^K w_{ik}^{1/\alpha} Z_{kt}} - m \right)^{-2} \left( - \frac{x_{it} w_{ik}^{1/\alpha}}{(\sum_{k=1}^K w_{ik}^{1/\alpha} Z_{kt})^2} \right) \right] \end{aligned}$$

## C.1 extVAE details

We use similar idea to build another encoder for estimating the tilting index. The weight and bias parameters in this encoder are equipped with tildes:

$$\tilde{\mathbf{z}}_t = \tilde{\boldsymbol{\mu}}_t + \tilde{\boldsymbol{\sigma}}_t \tilde{\boldsymbol{\epsilon}}_t,$$

with

$$\tilde{\boldsymbol{\epsilon}}_t \stackrel{iid}{\sim} MVN(\mathbf{0}_k, \text{Diag}_k(1)).$$

The two-layers perceptron neural networks have the form of:

$$\begin{aligned} \boldsymbol{\mu}_t &= \text{relu}(\mathbf{W}_4 \mathbf{h}_1 + \mathbf{b}_4), & \tilde{\boldsymbol{\mu}}_t &= \tilde{\mathbf{W}}_4 \tilde{\mathbf{h}}_1 + \tilde{\mathbf{b}}_4, \\ \log \boldsymbol{\sigma}_t^2 &= \mathbf{W}_3 \mathbf{h}_1 + \mathbf{b}_3, & \log \tilde{\boldsymbol{\sigma}}_t^2 &= \tilde{\mathbf{W}}_3 \tilde{\mathbf{h}}_1 + \tilde{\mathbf{b}}_3, \\ \mathbf{h}_1 &= \text{relu}(\mathbf{W}_2 \mathbf{h} + \mathbf{b}_2), & \tilde{\mathbf{h}}_1 &= \text{relu}(\tilde{\mathbf{W}}_2 \tilde{\mathbf{h}} + \tilde{\mathbf{b}}_2), \\ \mathbf{h} &= \text{relu}(\mathbf{W}_1 \mathbf{x}_t + \mathbf{b}_1), & \tilde{\mathbf{h}} &= \text{relu}(\tilde{\mathbf{W}}_1 \mathbf{x}_t + \tilde{\mathbf{b}}_1) \end{aligned}$$

in which  $\phi_e = (\mathbf{W}_1, \mathbf{W}_2, \mathbf{W}_3, \mathbf{W}_4, \mathbf{b}_1, \mathbf{b}_2, \mathbf{b}_3, \mathbf{b}_4, \tilde{\mathbf{W}}_1, \tilde{\mathbf{W}}_2, \tilde{\mathbf{W}}_3, \tilde{\mathbf{W}}_4, \tilde{\mathbf{b}}_1, \tilde{\mathbf{b}}_2, \tilde{\mathbf{b}}_3, \tilde{\mathbf{b}}_4)$ . Both  $\mathbf{W}_1$  and  $\tilde{\mathbf{W}}_1$  are  $K \times n_s$  weight matrices which encoding the information from  $\mathbf{X}$  to  $K$ -dimensional space and  $K$  is the total number of pre-specified knots,  $\mathbf{W}_2, \mathbf{W}_3, \mathbf{W}_4, \tilde{\mathbf{W}}_2, \tilde{\mathbf{W}}_3, \tilde{\mathbf{W}}_4$  are  $K \times K$  matrices, and  $\mathbf{b}_1, \mathbf{b}_2, \mathbf{b}_3, \mathbf{b}_4, \tilde{\mathbf{b}}_1, \tilde{\mathbf{b}}_2, \tilde{\mathbf{b}}_3, \tilde{\mathbf{b}}_4$  are  $K \times 1$  vectors.

For the decoder, we assume for  $t = 1, \dots, n_t$  and  $j = 1, \dots, n_s$

$$\begin{aligned} \Pr(\mathbf{X}_t \leq \mathbf{x}_t \mid \mathbf{Z}_t, \phi_d) &= \exp \left\{ -(\tau^{1/\alpha_0} \mathbf{x}_t^{-1/\alpha_0})^T \mathbf{y}_t \right\}, \\ \log p_{\phi_d}(\mathbf{z}_t) &= \sum_{k=1}^K \log H(z_{kt}; \alpha, \alpha, \theta_{kt}), \end{aligned} \tag{22}$$

in which  $\boldsymbol{\Omega}$  is a  $n \times K$  matrix whose  $j$ th row is  $(w_{1j}, \dots, w_{Kj})$  and

$$\begin{aligned} \mathbf{y}_t &= \boldsymbol{\Omega}^{1/\alpha} \mathbf{z}_t, & n \times K \\ \alpha_t &= \text{relu}(W_8 \mathbf{l}_1 + \mathbf{b}_8), & p \times K \\ \boldsymbol{\theta}_t &= \text{relu}(W_7 \mathbf{l}_1 + \mathbf{b}_7), & p \times K \\ \mathbf{l}_1 &= \text{relu}(W_6 \mathbf{l} + \mathbf{b}_6), & K \times K \\ \mathbf{l} &= \text{relu}(W_5 \mathbf{z}'_t + \mathbf{b}_5), & K \times K \end{aligned} \tag{23}$$

We denote all decoder parameters by  $\phi_d = (W_5, W_6, W_7, W_8, \mathbf{b}_5, \mathbf{b}_6, \mathbf{b}_7, \mathbf{b}_8, \alpha_0, \tau, \boldsymbol{\Omega})$ .

In generating the latent variables  $\mathbf{z}$  and  $\mathbf{z}'$ , we use the reparameterization trick (see Section 2.4 in [Kingma et al., 2019](#), for details) with auxiliary variables  $\boldsymbol{\epsilon}$  and  $\boldsymbol{\epsilon}'$  which are independent of  $\mathbf{x}$  or  $\boldsymbol{\phi}$ :

$$\begin{aligned} \mathbf{z}_t &= \boldsymbol{\mu}_t + \boldsymbol{\sigma}_t \boldsymbol{\epsilon}_t \\ \mathbf{z}'_t &= \boldsymbol{\mu}'_t + \boldsymbol{\sigma}'_t \boldsymbol{\epsilon}'_t \end{aligned} \tag{24}$$

with

$$\begin{aligned}\boldsymbol{\epsilon}_t &\sim N(0, I) \\ \boldsymbol{\epsilon}_t' &\sim N(0, I)\end{aligned}$$

The optimization objective of the variational autoencoder is to maximize the evidence lower bound (ELBO):

$$\begin{aligned}\mathcal{L}_{\phi_d, \phi_e}(\mathbf{x}_t) &= E_{q_{\phi_e}(\mathbf{z}_t|\mathbf{x}_t)} \left\{ \log \frac{p_{\phi_d}(\mathbf{x}_t, \mathbf{z}_t)}{q_{\phi_e}(\mathbf{z}_t|\mathbf{x}_t) \cdot q_{\phi_e}(\mathbf{z}_t'|\mathbf{x}_t)} \right\} \\ &= \log p_{\phi_d}(\mathbf{x}_t, \mathbf{z}_t) - D_{KL}\{q_{\phi_e}(\mathbf{z}_t|\mathbf{x}_t) || p_{\phi_d}(\mathbf{z}_t|\mathbf{x}_t)\}.\end{aligned}$$

and we have spatial location  $j \in \{1, \dots, n_s\}$ , time points  $t \in \{1, \dots, n_t\}$  and knot  $k \in \{1, \dots, K\}$ . For now we also fix  $\alpha$  in exponentially tilted distribution and  $W$  matrix which is the Wendland basis function with 2 dimensions (i.e  $s = 2$ ) and smoothness of 2 (i.e  $k = 1$ ), then the ELBO is like:

$$\begin{aligned}\mathcal{L}_{\phi_d, \phi_e}(\mathbf{x}_t) &= E_{q_{\phi_e}(\mathbf{z}_t|\mathbf{x}_t)} \left\{ \log \frac{p_{\phi_d}(\mathbf{x}_t, \mathbf{z}_t)}{q_{\phi_e}(\mathbf{z}_t|\mathbf{x}_t) \cdot q_{\phi_e}(\mathbf{z}_t'|\mathbf{x}_t)} \right\} \\ &= \log(p_{\phi_d}(\mathbf{x}_t, \mathbf{z}_t)) - \log(q_{\phi_e}(\mathbf{z}_t|\mathbf{x}_t)) - \log(q_{\phi_e}(\mathbf{z}_t'|\mathbf{x}_t))\end{aligned}$$

with

$$\begin{aligned}\log(p_{\phi_d}(\mathbf{x}_t, \mathbf{z}_t)) &\propto \log \left( p(\mathbf{X}_t = \mathbf{x}_t | \mathbf{z}_t) \cdot p(\mathbf{z}_t | \boldsymbol{\theta}_t) \cdot p(\boldsymbol{\theta}_t) \right) \\ &= \log \left( \left( \frac{1}{\alpha} \right)^{n_s} \left( \prod_{j=1}^{n_s} y_{jt} x_{jt}^{-1/\alpha-1} \right) \exp \left[ - \sum_{j=1}^{n_s} y_{jt} x_{jt}^{-1/\alpha} \right] \right) \\ &\quad + \sum_{k=1}^K \log H(z_{kt}; \alpha, \alpha, \theta_{kt}), \\ \log(q_{\phi_e}(\mathbf{z}_t|\mathbf{x}_t)) &\propto - \sum_{k=1}^K \left\{ \frac{\epsilon_{kt}^2}{2} + \log(\sigma_{kt}) \right\}, \\ \log(q_{\phi_e}(\mathbf{z}_t'|\mathbf{x}_t)) &\propto - \sum_{k=1}^K \left\{ \frac{\epsilon_{kt}'^2}{2} + \log(\sigma_{kt}') \right\},\end{aligned}$$

and we followed calculation steps in Appendix 4 of [Bopp et al. \(2021\)](#) to calculate log-likelihood of exponentially tilted distribution  $H(\alpha, \alpha, \theta)$  while applying Monte Carlo integration for the integral approximation.

The ELBO of sample  $\mathbf{x}$  for all time points is:

$$\begin{aligned}\mathcal{L}_{\phi_d, \phi_e}(\mathbf{x}) &= E_{q_{\phi_e}(\mathbf{z}|\mathbf{x})} \left\{ \sum_{t=1}^{n_t} \log \frac{p_{\phi_d}(\mathbf{x}_t, \mathbf{z}_t)}{q_{\phi_e}(\mathbf{z}_t|\mathbf{x}_t) \cdot q_{\phi_e}(\mathbf{z}'_t|\mathbf{x}_t)} \right\} \\ &\propto -n_s n_t \log \alpha + \sum_{t=1}^{n_t} \sum_{j=1}^{n_s} \left( \log(y_{jt} x_{jt}^{-1/\alpha-1}) - y_{jt} x_{jt}^{-1/\alpha} \right) \\ &\quad + \sum_{t=1}^{n_t} \sum_{k=1}^K \{ \log H(z_{kt}; \alpha, \alpha, \theta_{kt}) + z_{kt} \} + \sum_{t=1}^{n_t} \sum_{k=1}^K \left\{ \frac{\epsilon_{kt}^2}{2} + \log(\sigma_{kt}) + \frac{\epsilon_{kt}^{2'}}{2} + \log(\sigma'_{kt}) \right\}\end{aligned}$$

## C.2 Finding start values

In finding a reasonable starting values of parameters in CVAE, the naive way is doing projection to our model to find a good approximation of  $w_1$  and let the rest parameters be non-informative which can be trained through the data.

$$\hat{W}_1 = ((W_{\alpha}^{\frac{1}{\alpha}})^T W_{\alpha}^{\frac{1}{\alpha}})^{-1} (W_{\alpha}^{\frac{1}{\alpha}})^T \varepsilon$$

where

$$\varepsilon = \begin{bmatrix} \frac{1}{\frac{1}{T} \sum_{t=1}^T \epsilon_t(s_1)} & & 0 \\ & \ddots & \\ 0 & & \frac{1}{\frac{1}{T} \sum_{t=1}^T \epsilon_t(s_{n_s})} \end{bmatrix}$$

Then we can plug  $\hat{W}_1$  into the decoder to get a initial latent variable  $\hat{\mathbf{z}}_t$ . Then we optimize the log-likelihood of  $P(X_t = \mathbf{x}_t | \hat{\mathbf{z}}_t)$  to get a good initial  $\hat{\mathbf{z}}_t^{(0)}$ . Assume that

$$\hat{\mathbf{z}}^{(0)} = W_1^{(0)} X$$

then apply QR decomposition to solve for  $W_1^{(0)}$ . For the rest of parameters, their setups

are as follows:

$$\begin{aligned}
W_2^{(0)} &= \text{Diag}(1), & K \times K \\
W_3^{(0)} &= \text{Diag}(0), & K \times K \\
W_4^{(0)} &= \text{Diag}(1), & K \times K \\
\mathbf{b}_1^{(0)} &= (0, \dots, 0)^T, & K \times 1 \\
\mathbf{b}_2^{(0)} &= (0.00001, \dots, 0.00001)^T, & K \times 1 \\
\mathbf{b}_3^{(0)} &= (-3, \dots, -3)^T, & K \times 1 \\
\mathbf{b}_4^{(0)} &= (0, \dots, 0)^T, & K \times 1 \\
W_1'^{(0)} &= W_1^{(0)}, & K \times n_s \\
W_2'^{(0)} &= \text{Diag}(1), & K \times K \\
W_3'^{(0)} &= \text{Diag}(0), & K \times K \\
W_4'^{(0)} &= \text{Diag}(1), & K \times K \\
\mathbf{b}_1'^{(0)} &= (0, \dots, 0)^T, & K \times 1 \\
\mathbf{b}_2'^{(0)} &= (0.05, \dots, 0.05)^T, & K \times 1 \\
\mathbf{b}_3'^{(0)} &= (-10, \dots, -10)^T, & K \times 1 \\
\mathbf{b}_4'^{(0)} &= (0, \dots, 0)^T, & K \times 1 \\
\\ 
W_5^{(0)} &= \text{Diag}(1), & K \times K \\
W_6^{(0)} &= \text{Diag}(1), & K \times K \\
W_7^{(0)} &= \text{Diag}(1), & K \times K \\
\mathbf{b}_5^{(0)} &= (10^{-6}, \dots, 10^{-6})^T, & K \times 1 \\
\mathbf{b}_6^{(0)} &= (10^{-6}, \dots, 10^{-6})^T, & K \times 1 \\
\mathbf{b}_7^{(0)} &= (10^{-6}, \dots, 10^{-6})^T, & K \times 1
\end{aligned}$$

Then plug in the encoder structure in 3 to get  $\hat{\boldsymbol{\mu}}_t$  and  $\hat{\boldsymbol{\sigma}}_t$ , and calculate  $\hat{\mathbf{v}}_t$  via 24. The initial value of  $\mathbf{b}_8$  can be obtained by

$$\mathbf{b}_8^{(0)} = -\text{relu}(W^{\frac{1}{\alpha}} \hat{\mathbf{v}}_t - X)$$